Bioactive Materials 43 (2025) 603–618

Contents lists available at ScienceDirect

Bioactive Materials

journal homepage: www.keaipublishing.com/en/journals/bioactive-materials

Development of an implantable sensor system for *in vivo* strain, temperature, and pH monitoring: comparative evaluation of titanium and resorbable magnesium plates

A.M. Rich [a,*], W. Rubin [a], S. Rickli [a,b], T. Akhmetshina [a], J. Cossu [a], L. Berger [a], M. Magno [b], K.M. Nuss [c], B. Schaller [d], J.F. Löffler [a,**]

[a] Laboratory of Metal Physics and Technology, Department of Materials, ETH Zurich, 8093 Zurich, Switzerland
[b] Department of Information Technology and Electrical Engineering, ETH Zurich, 8092 Zurich, Switzerland
[c] Musculoskeletal Research Unit, Vetsuisse Faculty, University of Zurich, 8057 Zurich, Switzerland
[d] Inselspital, Bern University Hospital, 3010 Bern, Switzerland

ARTICLE INFO

Keywords:
Implantable sensors
Biodegradable metals
Magnesium
Fracture fixation
pH
Strain

ABSTRACT

Biodegradable magnesium is a highly desired material for fracture fixation implants because of its good mechanical properties and ability to completely dissolve in the body over time, eliminating the need for a secondary surgery to remove the implant. Despite extensive research on these materials, there remains a dearth of information regarding critical factors that affect implant performance in clinical applications, such as the *in vivo* pH and mechanical loading conditions. We developed a measurement system with implantable strain, temperature, pH and motion sensors to characterize magnesium and titanium plates, fixating bilateral zygomatic arch osteotomies in three Swiss alpine sheep for eight weeks. pH 1–2 mm above titanium plates was 6.6 ± 0.4, while for magnesium plates it was slightly elevated to 7.4 ± 0.8. Strains on magnesium plates were higher than on titanium plates, possibly due to the lower Young's modulus of magnesium. One magnesium plate experienced excessive loading, which led to plate failure within 31 h. This is, to our knowledge, the first *in vivo* strain, temperature, and pH data recorded for magnesium implants used for fracture fixation. These results provide insight into magnesium degradation and its influence on the *in vivo* environment, and may help to improve material and implant design for future clinical applications.

1. Introduction

Biodegradable magnesium implants are widely investigated because of their favorable properties for fracture fixation. They can support bone during fracture healing and then dissolve over time, eliminating the potential need for a secondary surgery. While Mg alloys for such applications have been investigated extensively, *in vivo* data quantifying some important degradation parameters are generally lacking. Conditions of the corrosive environment such as pH and temperature have a profound effect on magnesium degradation. The variety of *in vitro* experimental setups has led to significant spread in results between experiments, groups, and especially when compared to *in vivo* data [1]. Changing the composition or temperature of the media can greatly influence the degradation rate [1–3]. While Mg degradation is influenced by the corrosive environment, its dissolution can also change that environment. For example, Mg degradation locally increases the pH *in vitro* [4]; whether this local pH increase also occurs *in vivo* remains unknown. While physiological pH is normally tightly controlled to be within 7.35–7.45 to maintain proper cellular function [5], local pH varies between 5.45–8.65 in response to trauma, such as surgery [6,7]. Wound healing and tissue regeneration are commonly accompanied by changes in pH to ranges outside of normal physiological conditions [8], but these factors are normally not taken into account when performing *in vitro* degradation tests. Clearly, the dynamic *in vivo* environment should be quantitatively accounted for when investigating Mg degradation. One study characterized the pH of magnesium implants and

Peer review under responsibility of KeAi Communications Co., Ltd.
* Corresponding author.
** Corresponding author.
E-mail addresses: andrea.rich@mat.ethz.ch (A.M. Rich), joerg.loeffler@mat.ethz.ch (J.F. Löffler).

https://doi.org/10.1016/j.bioactmat.2024.09.015
Received 12 March 2024; Received in revised form 10 September 2024; Accepted 12 September 2024

surrounding tissue *in vivo* using fluorescent imaging techniques [8]. This works only for subcutaneous implants and gives ranges of pH rather than precise values. Therefore, more localized pH measurements *in vivo* would provide data that is not currently available.

Temperature is also known to have an effect on magnesium degradation, with a temperature increase from 37 °C to 40 °C reported to increase corrosion rate by 50 % [9]. However, recent studies suggest that under conditions that mimic the physiological environment, an increase in temperature *in vitro* can decrease corrosion rate due to the formation of more stable corrosion products that protect the underlying Mg from the corrosive media [2]. Quantifying the *in vivo* temperature during bone healing may allow optimization of *in vitro* studies to further replicate physiological conditions. Additionally, the increase in blood flow to tissue post-operatively is thought to be accompanied by a localized temperature increase, which may have implications on Mg degradation. Temperature changes can also be indicative of an interruption in bone healing or infections, as reported in Ref. [10]. This study attempted to quantify the temperature change *in vivo* in human subjects using external imaging techniques [10], which, however, may not provide accurate localized results. Gathering localized *in vivo* data of temperature changes during fracture healing would elucidate whether this temperature change is clinically important and allow for inclusion of more accurate temperature data in laboratory testing.

Mechanical properties of magnesium may be favorable for fracture-fixation applications. With a Young's modulus (E) of 45 GPa, magnesium has mechanical properties more similar to bone ($E \sim$ 5–20 GPa [11]) than titanium ($E =$ 105 GPa [12]), which is expected to reduce stress shielding [13]. It is also well established that fracture healing depends on the bone's mechanical loading [14–21]; for fracture-fixation applications, the implant must be strong enough to initially fully support the bone fragments to enable healing and complete fracture consolidation. Thus, characterizing the mechanical conditions would provide valuable insights to improve implant materials and designs, and to understand how they impact fracture healing. Additionally, "smart" implants to monitor fracture healing are increasingly discussed in literature and are expected to gain wider clinical use in the near future [22–24]. Studies have been performed to measure mechanical forces on bone directly [25–28]; on the face of fracture-fixation devices [14,15,29,30]; and inside of larger (hip, knee, shoulder) implants [31–34] using various sensors such as strain gauges. While numerous data exists for permanent implants, no studies to date have collected *in vivo* loading data for degradable metallic implants. As their mechanical properties differ fundamentally from permanent implants, quantifying their *in vivo* loading and effects on fracture healing would provide invaluable data in the area of biodegradable implant applications.

Since the magnesium substrate is degrading, it presents unique challenges for *in vivo* strain gauge measurements not seen for permanent implant applications. Strain gauges need to stay securely glued to the surface to measure accurately, and protection from body fluids is necessary for long-term measurements. Therefore, modifying the magnesium alloy itself to be less reactive (enhancing the adhesion of the gauges) and placing coatings on top of the sensors both help to facilitate these measurements. Plasma electrolytic oxidation (PEO) is a process where an oxide layer is grown on a metal substrate via a plasma discharge that is created while it is submerged in an electrolyte. This forms a strongly adhered ceramic coating (MgO) on the metal surface that can slow corrosion by protecting the underlying metal substrate from the corrosive media [35,36]. PEO is increasingly used on biodegradable magnesium alloys to slow the initial degradation and hydrogen gas release, and thus to improve clinical outcomes in animal studies [37–41]. An additional coating to cover the sensors is also necessary to make them waterproof and biocompatible. Parylene is a polymer commonly used in the implantable medical device industry as a moisture barrier and for corrosion prevention of sensitive electronic components [42–49]. Studies investigating parylene as a coating for orthopedic implants showed promising results for titanium and stainless-steel devices [42,50–52] and recently as a corrosion-resistant coating on various magnesium alloys [53–55]. However, long-term *in vitro* and *in vivo* investigations of parylene on magnesium alloys are lacking in the literature. As a biocompatible, corrosion-resistant encapsulant for both electronics and orthopedic implants, parylene offers a unique opportunity when developing implantable sensors for biodegradable magnesium alloys. We tested parylene-C coating and a hybrid PEO + parylene-C coating on Mg to determine their suitability for *in vivo* sensor applications.

To address the lack of data quantifying the *in vivo* degradation conditions and mechanical performance of biodegradable implants and to carry out an accurate in-field evaluation, we developed a fully implantable measurement system to record temperature, pH, and strain *in vivo* on implant plates of a magnesium–calcium alloy (X0, MgCa0.45, in wt.%, PEO coated) and titanium (grade-2), which served as reference. Apparently, this is the first strain, pH, and temperature data recorded from degrading Mg implants *in vivo* and could help quantifying the complex mechanical and environmental conditions that affect degradation and fracture healing. Data presented in this work provides insight into the conditions surrounding magnesium degradation *in vivo* and could be used to improve Mg-based implants for future clinical applications.

2. Materials and methods

2.1. Implant manufacturing

The magnesium alloy X0 (MgCa0.45, in wt%) was made from ultrahigh-purity Mg (99.999 %) [56] and Ca (99.95 wt%). The exact composition and impurity content were determined with inductively coupled plasma optical emission spectroscopy (ICP-OES) and glow discharge mass spectrometry (GDMS), respectively. Mg was alloyed with Ca in an induction furnace at 750 °C under a protective argon atmosphere with at least 5N purity to form a billet. The billet was homogenized at 350 °C for 12 h, solutionized at 450 °C for 8 h, and then quenched in water. Indirect extrusion was deployed to produce material for screws (6 mm diameter) and plates (9 mm × 3.5 mm rectangular cross section), which were then machined to the final dimensions. Titanium plates were machined from grade-two titanium (Bibus Metals AG, Fehraltorf, Switzerland) as specified in ASTM B265 – 20a, which is at least 99.5 wt% titanium. Standard titanium screws were used to fixate the titanium plates (MatrixMANDIBLE™ D2.0 mm, Synthes). The final dimensions were 46.2 × 6.75 × 1.8 mm^3 for the Mg plates and 46.4 × 5.0 × 1.0 mm^3 for the Ti plates.

The Mg plates and screws were PEO coated at the Robert Mathys Foundation, Switzerland. They were attached to customized sample holders and submerged in an electrolyte containing diammonium hydrogen phosphate (0.05 M), urea (1 M), and ammonium hydroxide (1.07 M) [57]. Direct current was applied with a density of 14 mA/cm^2 until the voltage reached 400 V and held for 5 min. The samples were removed from the electrolyte, immersed in deionized water for 6–10 min, rinsed with ethanol, and then dried in a 60 °C oven for at least 20 min. Coating thickness was determined via eddy current measurements (Fischer Dualscope FMP20) of witness parts that were coated simultaneously with the plates and screws; it is reported as mean and standard deviation of 10 measurements.

2.2. Sensor design

Four semiconductor strain gauges (SS-027-013–500 P, Micron Instruments, Simi Valley, USA) with a nominal resistance of 540 ± 50 Ohms and a gauge factor of 155 ± 10 were glued to a custom-designed, 3 mm × 3 mm FR-4 flexible backing (HAPTICA SRL, Italy) and configured as two independent Wheatstone half-bridges. They were configured to measure axial loading (tension/compression) and in-plane bending.

The pH sensor consists of an ion-sensitive field effect transistor

(ISFET) that has a sensing area of 1.2 × 3 mm^2 with a 2 mm diameter Ag/AgCl reference electrode combined in a 10 mm diameter package (MSFET3351, Microsens SA, Switzerland). Operation with a constant drain-source voltage of 0.5 V and a drain current of 50 μA ensured that the gate-source voltage linearly depends on pH [58]. The signal was amplified with a gain of 3.6 to maximize input voltage in a range of 0–1.8 V for pH 4.8–9, giving a maximum resolution of 2.4 mpH.

2.3. Measurement system

The measurement system consists of a battery-powered energy-efficient embedded system with a custom printed circuit board (PCB) and cables made from a stretchable polyurethane material that connect the sensors to the PCB (Fig. 1). The instrumented plates were used to fixate bilateral zygomatic arch osteotomies in three female alpine sheep for eight weeks. Data was collected autonomously from the sensors for 10 s every hour, and downloaded and analyzed following sacrifice of the animals after eight weeks. Per animal, one Mg plate and one Ti plate outfitted with the measurement systems were implanted, i.e., six measurement systems were implanted into three animals.

The PCB was manufactured with four copper layers and a nominal thickness of 0.6 ± 0.1 mm (PCBWay, Shenzhen, China). Cables (Würth Elektronik, Germany) were designed with two copper layers embedded in a stretchable polyurethane material. The copper traces were routed with a custom-designed meander pattern, maintaining stretchability of the cable and mechanical integrity of the copper.

The embedded system's firmware was deployed and executed on a microcontroller (STM32L422RBI6, STMicroelectronics) that interfaced with the sensors and memory. Strain gauges were sampled with a 24-bit differential analog-to-digital converter (ADS1220, Texas Instruments)

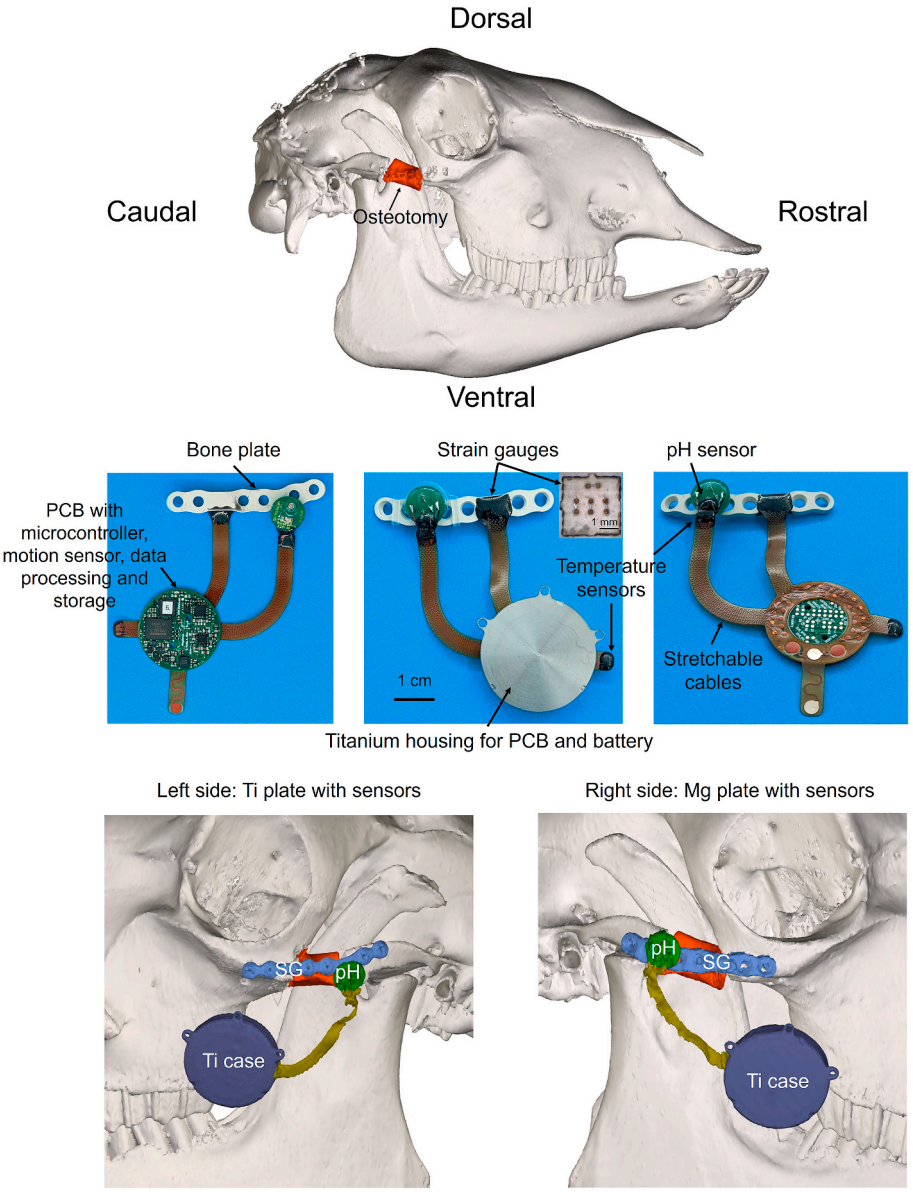

Fig. 1. Measurement system and implantation location. Top row: 3D render of CT scan, showing the location of the fully-mobilized zygomatic arch osteotomy on the right side of a sheep's skull. Middle row: A fully-assembled sensor system with a magnesium plate. Strain gauges were glued to the upper surface of the rostral ridge and coated with polyurethane (inset: strain gauges before coating). Temperature sensors were placed at the osteotomy site and at a reference location. A pH sensor was attached to the plate with a clamp close to the caudal osteotomy line. Stretchable cables connect the sensors and battery to the printed circuit board (PCB). A titanium case houses the PCB and battery and was placed subcutaneously. Bottom row: 3D render of a CT scan showing the implantation locations of titanium (left) and magnesium (right) plates together with the strain gauge (SG) and pH sensors in one animal.

with a sampling rate of 175 Hz and gain of 8. The pH sensors were sampled at 640.5 Hz for 1 s using an internal 12-bit ADC of the microcontroller and the average value was stored. An inertial measurement unit (IMU) with integrated triaxial accelerometer and gyroscope (LSM6DSLTR, STMicroelectronics) was used to record acceleration and was sampled at 208 Hz with a range of ±2 *g*. Two digital temperature sensors with an accuracy of ±0.1 °C (TMP117, Texas Instruments) were used to record the average of 8 samples collected at 65 Hz from osteotomy and reference locations. The osteotomy sensors were above the caudal osteotomy line and the reference sensors were placed approximately 60 mm away. All data was written to a 1 G-bit NAND flash chip (W25N01GWZEIG, Winbond), serving as nonvolatile memory where the data was saved until the sensors were explanted. A 3 V lithium coin cell battery (CR2320, Renata) with a capacity of 150 mA h was used to power system. A simplified circuit diagram is shown in Fig. 2.

2.4. System assembly

Prior to attaching the strain gauges, the plates were bent to match the curvature of a 3D printed reference skull created from a CT scan of an

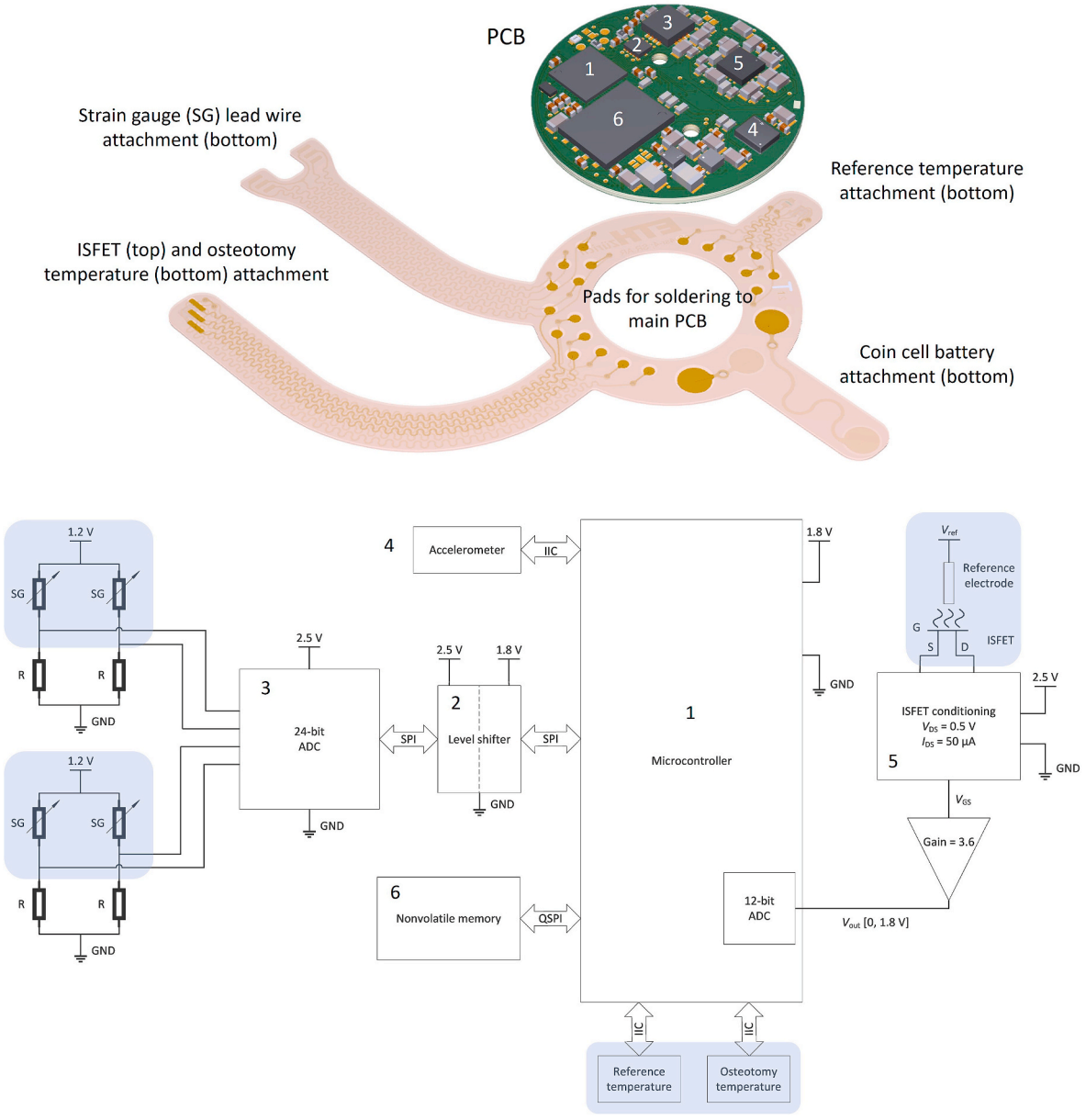

Fig. 2. Simplified circuit diagram. Components are shown in the 3D rendering (top) of the printed circuit board (PCB) and labeled by number corresponding to the schematic (bottom). Their voltage requirements and communication protocols are also shown. Blue boxes indicate components attached to the stretchable cables as shown in the top 3D rendering. Strain gauges (SG) were glued to the magnesium and titanium plates as two Wheatstone half-bridges, with bridge completion resistors (R) soldered to the PCB inside the titanium case. One bridge was used to measure axial loading and the other for measuring in-plane bending, by gluing the gauges appropriately. They were sampled with a 24-bit analog-to-digital converter (ADC, 3) that was converted to the correct voltage level (using the level shifter, 2) and communicated with the microcontroller (1) using the serial peripheral interface (SPI). The temperature sensors at two locations (osteotomy and reference) and the accelerometer (4) were read using the inter-integrated circuit (IIC) bus. The pH sensor (ISFET), whose gate-source voltage (V_{GS}) was conditioned to linearly depend on pH (5), was amplified with a gain of 3.6 and read using a 12-bit ADC internal to the microcontroller. Data was stored in nonvolatile memory (6) using the quad serial peripheral interface (QSPI).

anatomically similar sheep. This ensures that the plate can be applied to the bone without intraoperative bending, which may damage the mounted strain gauges, and increases the likelihood of a well-fitting plate. The plates were cleaned with isopropanol, then the backed strain gauges were glued with epoxy (353ND, EPO-TEK) and cured at 150 °C for 1 h. Cables were glued to the Mg and Ti plates using polyurethane resin (UR5118, Electrolube) and cured at 65 °C for 4 h. The strain gauge and pH lead wires were soldered to pads on the cables with low-temperature solder paste. The battery was attached using a conductive silver epoxy (8330 S, MG Chemicals) and cured at 65 °C for 2 h. The pH sensors were then attached to the plates using 3D printed clamps that fixed the ISFET approximately 1 mm from the plates' surface.

The devices were programmed to record strain, temperature and pH every hour starting at 8 a.m. CET on the day of implantation. The PCB and battery were placed in a titanium case (with slots for the cables to exit), which was screwed shut and sealed with an O-ring. Polyurethane resin was added to the perimeter of the case and on top of the strain gauges, temperature sensors, and pH-sensor solder joints and cured. A final 10 μm layer of parylene-C was applied everywhere except the pH sensor electrodes and non-gauged regions of the plates; it was applied along approximately 2 cm of the plates, including the area where the strain gauges were glued and the adjacent screw holes.

2.5. Sensor calibration

For strain gauge calibration, a custom-designed 4-point bending rig with a span of 6.0 mm (top) and 18.3 mm (bottom) was used. The gauged area was placed between the supports, which were loaded with weights to achieve applied loads of 7.5 N, 16 N, 40 N, and 53 N. The "tensile" loading direction was tested by placing the gauged surface pointing downwards, then the "bending" direction was measured by rotating the plate 90° and repeating the loading/unloading sequence. Data was collected at 175 Hz for 10 s every 15 s up to 3 min per load.

The applied moments were calculated based on the load and geometry of the bending test, and the theoretically expected strains (ε) were calculated using the geometrical properties of the plates and the locations of the gauges:

$$\varepsilon = \frac{12\,My}{Ebh^3} \tag{1}$$

where M is the bending moment, y is the distance of the gauges from the neutral axis, b and h are the respective width and thickness of the plate, and E is the Young's modulus of the implant material (105 GPa for Ti and 45 GPa for Mg).

To calibrate the pH sensors, sodium dihydrogen phosphate (NaH_2PO_4), disodium hydrogen phosphate (Na_2HPO_4), and sodium chloride (NaCl) were mixed to create calibration buffers with pH 5, 7, 7.4, and 8.3. To condition the dry sensors, we soaked them for 30 min in the pH 7 buffer. Then, the sensors were immersed in pH 7, 5, and 8.3 buffers and one datapoint was recorded every 15 s for 5 min, rinsing the sensors with deionized water in between. A calibration curve was created by averaging the voltage recorded in each buffer and fitting a linear line through the points. To determine temperature effects, a sensor was calibrated at 37 °C by heating the buffers in a water bath. The change in voltage as the sensor was heated from 23 °C to 37 °C in the pH 7 buffer was also measured. On the day of surgery, the pH sensors were soaked in a room-temperature pH 7.4 buffer for at least 15 min before activation, to condition the sensors. When the devices automatically turned on at the pre-set time, the voltage was recorded in the pH 7.4 buffer and used to perform an additional offset calibration. Temperature compensation was applied later during data analysis.

2.6. Enhanced coatings for long-term measurement stability

We tested parylene-C coating and a hybrid PEO + parylene-C coating on Mg substrates *in vitro* to determine their suitability for *in vivo* sensor applications; a strongly adhered coating that prevents corrosion is necessary for the strain gauges to measure properly. The mechanical stability of single (10 μm parylene coating) and hybrid coatings (PEO coating + 10 μm parylene coating) on X0 magnesium alloy samples was investigated through scratch and linear reciprocating ball-on-flat sliding wear tests using a tribometer (UMT TriboLab, Bruker) with a 20 N load cell under unlubricated conditions. Nine tests were conducted for each coating type. To ensure accurate measurements, the samples were securely fixed on a custom-designed sample holder to prevent motion and tilt. Prior to testing, surface contaminants were removed by wiping the surface with an ethanol-soaked tissue and an air-jet. The experiments were conducted in a controlled laboratory environment with a temperature of 22.6 ± 0.2 °C and a relative humidity of 49.8 ± 1.7 % ($n = 78$).

For scratch testing, a Rockwell C diamond stylus (spherical tip, 0.2 mm radius, 120° apex angle) was applied to the surface with a linearly increasing load from 0.1 N to 5 N along a 5 mm length with a speed of 5 mm/min. The first and second critical loads, L_{C1} and L_{C2}, representing cohesive and adhesive coating failure, were evaluated using high-resolution microscopy images (Leica VS700C) of the scratch tracks, cross-referenced with the respective load curves measured by the tribometer. The criteria defined in ASTM D7027 – 20, subsection 3.2.4.1, were used to determine the failure points in the scratch-track micrographs. For wear tests, an alumina sphere of 2 mm diameter (aluminum oxide sphere 99.7–2 mm Grad 10, Saphirwerk) was oscillated on the surface with a constant load of 5 N over a 4 mm wear track for 10 min at a sliding speed of 8 mm/s. The wear volume was assessed by analyzing the 3D profile of the wear track measured with a tactile profilometer (DektakXT, Bruker) using a custom MATLAB script. Scratch and wear testing was performed on hybrid-coated samples before and after immersion in simulated body fluid (SBF) for 4 weeks. SBF was mixed according to Table 1, adding the salts in the order of left to right to deionized water heated to 37 °C with a water bath (WB28, PolyScience). The pH was maintained between 7.3 and 7.5 using a CO_2 buffer system (Pro Flora pH Control Touch, JBL), which should closely mimic the *in vivo* environment [59]. Only hybrid samples were tested after immersion because those coated with only parylene experienced excessive corrosion underneath the parylene coating when immersed, which was considered unacceptable for *in vivo* application.

2.7. Animal experiments

Female Swiss alpine sheep (age 1.5–3.5 years, weight 55–90 kg) were used as experimental animals in this study, which was conducted in accordance with the Swiss laws of animal protection and welfare (license number ZH 121/20).

The sheep were acclimatized for at least 7 days before operation. Only animals with normal blood values and no signs of illness were included. They were group-housed in stables with at least 1.2 m^2 space per animal and allowed access to hay, mineral supplements and water ad libitum.

On the day of surgery, the animals were sedated with medetomidine (0.005–0.01 mg/kg bodyweight intramuscular), and buprenorphine (0.01–0.02 mg/kg BW i. m.) was injected for preemptive analgesia. Anesthesia was induced with ketamine (3–5 mg/kg BW intraveneous, i. v.), midazolam (0.1 mg/kg BW i. v.), and propofol (0.4–0.6 mg/kg BW or as needed i. v.). The animal was intubated and the anesthesia maintained by administering isoflurane (1–3 vol%) in oxygen via an adult F-circuit and a variable rate of infusion propofol (0.5–1 mg/kg/h) and ketamine (20–50 μg/kg/min). Vital signs were monitored intraoperatively and 5–10 ml/kg BW/h Ringer's lactate solution was administered.

After preparing the surgical site, 2.5 ml Ropivacain 0.5 % was

Table 1
Composition of simulated body fluid. The reagents were added in order from left to right into heated deionized water.

	1. KCl	2. NaCl	3. $NaHCO_3$	4. $MgSO_4{\cdot}7H_2O$	5. $CaCl_2{\cdot}2H_2O$	6. KH_2PO_4
Concentration (mg/l)	298.2	5844.0	2268.5	246.5	367.5	136.1

injected for local anesthesia. Ten minutes after injection, a skin incision was made, and bilateral zygomatic arch osteotomies were made sequentially. First, pilot holes were drilled at the desired locations in the bone using a custom drill guide. Then, the zygomatic arch bone was cut at two locations using a piezoelectric saw to create a completely mobile middle bone fragment (see Fig. 1). An Mg plate and six screws were used to fixate the right-sided defect, while a titanium plate and screws were used on the contralateral side. The sensor box was placed distally into the subcutaneous tissue. Care was taken to prevent damage to the sensors or cables during insertion. The skin was then closed in layers.

Postoperatively, buprenorphine (0.01–0.02 mg/kg BW) was injected i. m. every 4–6 h for analgesia for up to three days, paracetamol (10 mg/kg BW i. v.) BID-TID every 6–12 h if necessary, and carprofen (4 mg/kg BW, i. v.) SID for up to 5 days, depending on pain assessment. Intravenous prophylactic antibiotics (Penicillin 30,000 IU/kg BW, BID, i. v. and Gentamicin 4 mg/kg BW, SID, i. v.) were given on the day of surgery and for 4 days thereafter.

CT scans were performed immediately after surgery, and postoperatively at 2, 4, 6, and 8 weeks (± 1–4 days) to assess implant performance and bone healing. The 8-week CT scan was performed immediately after sacrifice.

2.8. Explantation and post-mortem analysis

After 8 weeks (± 1–4 days) the animals were sacrificed by an intravenous injection of pentobarbital (50–60 mg/kg BW). The implants, along with the bone and surrounding soft tissue, were removed with a saw. The samples were wrapped in saline-soaked gauze, stored in a polystyrene box with ice packs and transported for further analysis.

The sensor box was removed by cutting the cables connecting it to the pH sensor and strain gauges with a scalpel, leaving the plate, screws and surrounding soft-tissue undisturbed. MicroCT was performed on the remaining bone-plate construct with a resolution of 29.3 μm (Scanco Medical μCT 100 cabinet micro-CT scanner). Afterwards, the plates and screws were removed from the bone. The bone fragments were stored in a −80 °C freezer.

2.9. Data analysis

The sensor box was opened and the data was downloaded from the flash memory using a python script. The data was analyzed using the software package R (version 4.0.2), and the results are reported as mean ± standard deviation, unless otherwise stated.

Based on the circuit configuration and gauge layout, the voltage stored on the ADC was converted to strain (ε), using equation (2) for tension and equation (3) for bending:

$$\varepsilon_t = \frac{4V_r}{GF[(1+\nu) - 2V_r(\nu - 1)]} \tag{2}$$

$$\varepsilon_b = \frac{2V_r}{GF} \tag{3}$$

where V_r is the difference between the measured voltage and unstrained voltage (taken as the value when the device was activated and sitting on the table in the operating room), ν is Poisson's ratio (0.28), and GF is the gauge factor of 155.

The peak strains that occurred during dynamic loading, such as chewing, were calculated. First, the measurement periods that contain dynamic loading were identified by performing a fast Fourier transformation (FFT) on all measurement periods and selecting those that have frequencies greater than 1 Hz with a magnitude of at least 4 dB. The static component of the strain signal was removed for each period by creating a histogram of the recorded values and selecting the midpoint of the bin with the most values and subtracting it. Finally, the peaks were identified as those with a magnitude at least equal to the standard deviation of the signal and at least 25 samples apart.

The resultant acceleration R_{acc} was calculated from the x, y and z axes of the sensor according to $R_{acc} = \sqrt{x^2 + y^2 + z^2}$.

3. Results

3.1. Implant manufacturing

The exact Ca content of the alloy was determined to be 0.429 ± 0.005 wt% based on ICP-OES. The impurity analysis by GDMS is shown in Table 2, where only values above 0.1 ppm are shown. Via eddy-current measurements of witness parts, the PEO coating was estimated to have a thickness of 5.7 ± 0.7 μm. A full analysis of the coating was performed in a separate study [60]. Briefly, a dense coating layer of approximately 500 nm thickness borders the substrate, while the rest of the coating exhibits a porous microstructure. Top-view and cross-section micrographs of the PEO-coated screws used in this study are shown in the supplementary information (Fig. S1).

3.2. Enhanced polymeric coatings for long-term measurement stability

Compared to parylene-C alone, the hybrid PEO/parylene-C coating had significantly lower wear volume and significantly higher critical loads at failure (Tukey honest significant difference test, $p < 0.001$). After immersion, there was no significant difference in wear volume for the hybrid coating (hybrid immersed) compared to the values before immersion (Fig. 3a), while both critical loads, i.e. the cohesive and adhesive failure loads L_{C1} and L_{C2}, decreased after immersion ($p < 0.01$) (Fig. 3b). Fig. 3c shows the cohesive and adhesive failure loads on a scratch track of a hybrid-coated sample (non-immersed) using an optical microscope (top) and scanning electron microscope (bottom). Fig. S2 of the supplementary information further reveals that the hybrid samples, which were partially coated with parylene-C, are visually protected from degradation at least up to 4 weeks in SBF.

3.3. Sensor calibration and in vitro testing

Strain gauges were calibrated in both loading directions (Fig. 4a) and compared to theoretically calculated expected strains (Fig. 4b). For the tensile loading direction, the measured strains are in good agreement with the expected strains (slope = 1.03). In the bending direction, the measured strains are approximately 81 % of the maximum calculated strain (slope = 0.81), which could be attributed to the low length-to-depth ratio that makes bending theory less applicable. In both axes, the response is linear ($R^2 > 0.99$). One device was found to have reduced sensitivity compared to the other devices upon calibration, so a correction factor was applied to the calibration to compensate for this.

The average sensitivity of the six implanted pH sensors (including gain) was −221.48 ± 9.27 mV/pH at room temperature (an exemplary pH calibration curve is shown in Fig. 4c). Calibration at 37 °C showed a 4.7 % decrease in sensitivity versus 23 °C and an offset shift of 3.5 mpH/°C. These correction factors were applied to the room-temperature calibrations and the initial offset measurements of the implanted sensors when analyzing the *in vivo* data.

Table 2
Impurity analysis by glow discharge mass spectrometry. Values are given as ppm by weight and only values above 0.1 ppm are shown.

Element	Na	Al	Si	S	Cl	Cr	Mn	Fe	Ni	Cu	Zn	Pb
ppm	0.11	2.0	1.0	0.25	0.19	0.27	1.4	2.0	0.21	1.2	4.5	2.5

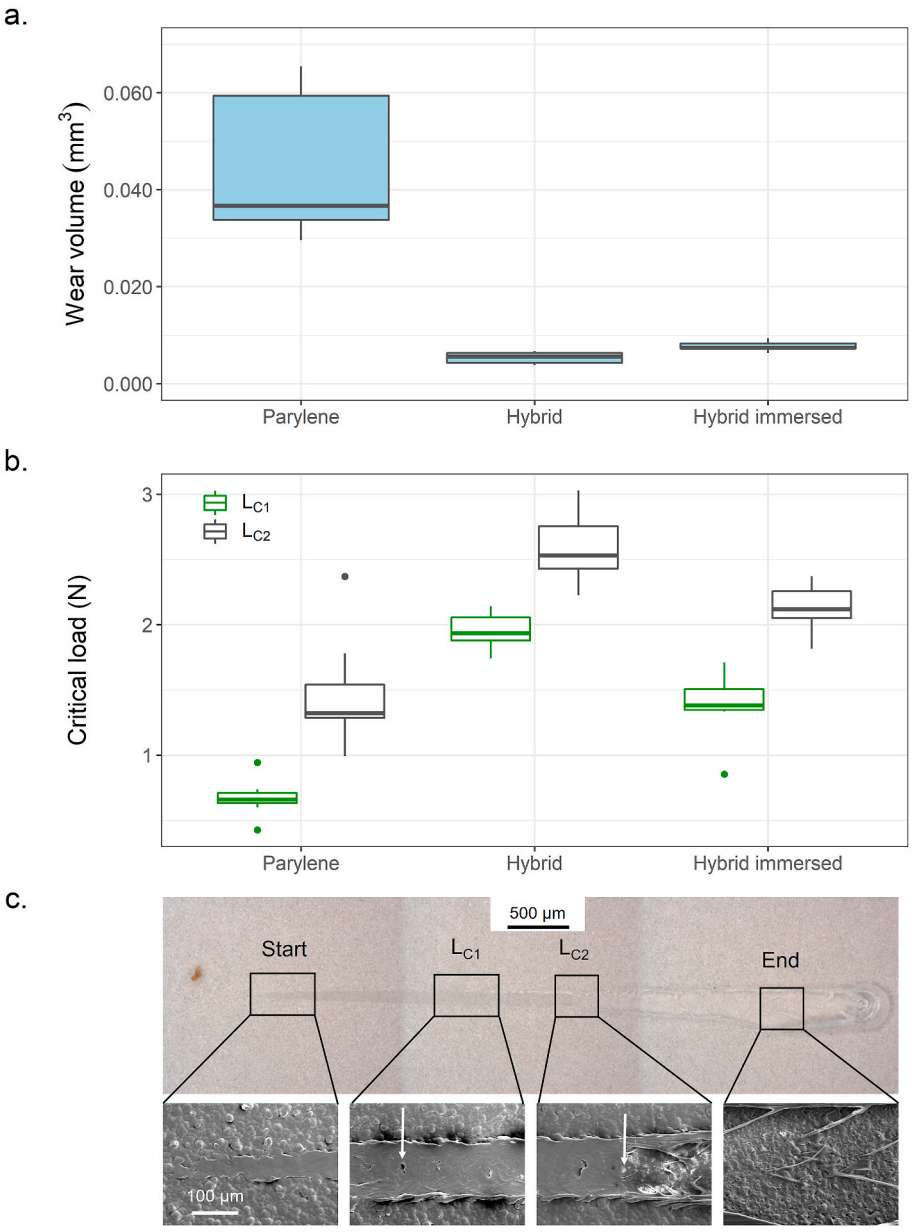

Fig. 3. Tribological testing of parylene-coated and hybrid-coated Mg alloy samples. a) Wear volume of X0 samples coated with parylene-C (parylene) and PEO + parylene-C (hybrid), as well as hybrid samples after four weeks of immersion in SBF (hybrid immersed). b) Critical loads representing cohesive (L_{C1}) and adhesive (L_{C2}) coating failure measured using a scratch test on parylene- and hybrid-coated X0 samples, and hybrid samples after immersion in SBF for four weeks. c) Scratch track of a hybrid-coated sample (non-immersed), showing the locations of L_{C1} and L_{C2} in an optical microscope (top) and scanning electron microscope (bottom).

3.4. Animal experiments

Six sensor systems (three for each implant material) were successfully implanted into three animals. No irregularities were noted during the surgeries and no complications were caused by the presence of the sensors. The two-week follow-up CT scan revealed that one magnesium plate broke close to the rostral osteotomy line of the created bone defect. Unrelated to this implant failure, the animal had to be sacrificed four weeks after surgery due to pathological blood values and gastrointestinal symptoms that could not be successfully treated. The remaining two sheep had no complications and were sacrificed eight weeks after surgery. At that timepoint, there were no signs of bone healing based on the CT or µCT scans for either the magnesium- or titanium-fixated osteotomies.

Data could be successfully downloaded from all six measurement systems. The titanium cases remained completely sealed, sufficiently protecting the PCBs and batteries from body fluids. Cracks were found in the parylene coating covering the cables, allowing body fluid to

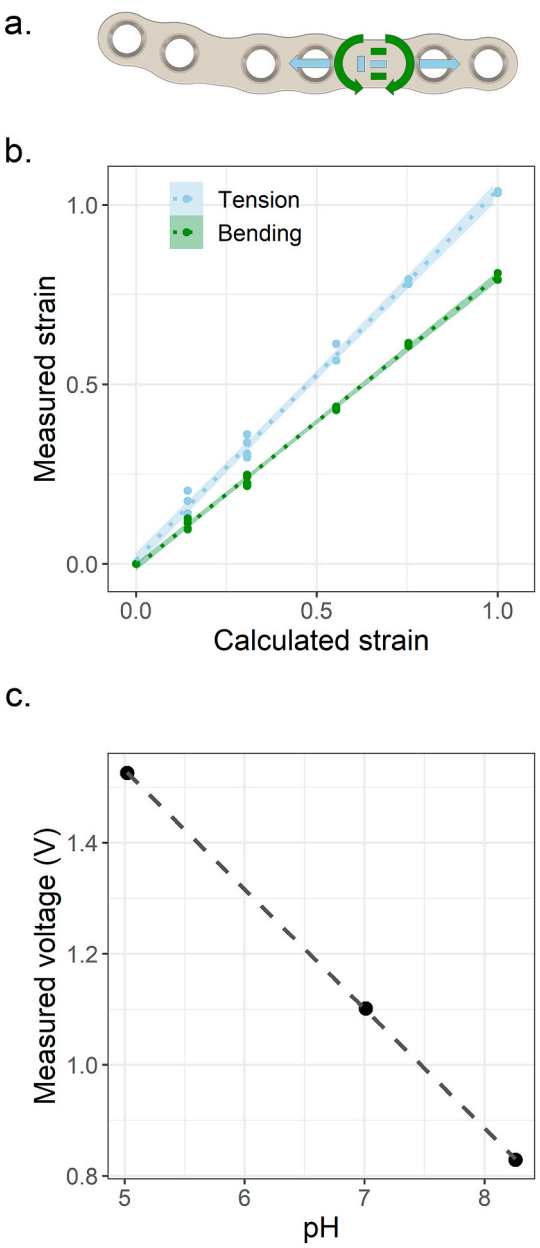

Fig. 4. Strain gauge and pH sensor calibration. a) Orientation of strain gauges on a magnesium plate and the corresponding measurement directions, with arrows pointing towards the positive direction. b) Strains measured during calibration versus theoretically calculated strains for one representative Mg and Ti device, normalized to calculated peak strain. c) Calibration of one pH sensor in phosphate-buffered saline solutions.

penetrate into the cables and causing the sensors to stop recording at various times (Table 3).

3.5. In vivo temperature

The average temperature at the osteotomy and refence locations were 37.6 ± 0.9 °C (n = 316) and 38.1 ± 0.6 °C (n = 1618), respectively. Grouped by implant material, the average temperatures across both locations were 37.8 ± 0.8 °C (n = 699) for magnesium and 38.1 ± 0.6 °C (n = 1235) for titanium. A two-way ANOVA with adjustment for multiple testing using Tukey's honest significant difference test revealed that the osteotomy temperature was significantly lower than the reference temperature, and that the titanium temperature was significantly higher than the magnesium temperature. There was also a significant interaction between the two variables ($p < 0.001$ in all cases).

Therefore, to assess if there was a local temperature change caused by the bone-healing response, we decoupled these effects by examining each implantation site specifically. For each measurement system (consisting of a reference sensor and osteotomy sensor), datapoints were considered where both sensors recorded data. Then, the difference between the reference and osteotomy sensors was calculated. Fig. 5a shows the average and standard deviation of the temperature difference (reference – osteotomy) for each implantation site separated by material type and averaged across all three sheep. The dashed vertical line at 12 h represents the last timepoint at which all temperature sensors were functioning (12 sensors total). Looking at the titanium plates, the reference temperature was 0.28 °C higher than the osteotomy temperature ($p < 0.01$, n = 167), while for the Mg plates, the reference temperature was 0.59 °C higher than the osteotomy temperature ($p < 0.001$, n = 148). The reference temperatures for Mg and Ti were 37.9 ± 0.9 °C (n = 148) and 38.2 ± 0.5 °C (n = 167), respectively, whereas the osteotomy temperatures for Mg and Ti were 37.3 ± 0.9 °C (n = 148) and 37.9 ± 0.9 °C (n = 167), respectively.

3.6. In vivo pH

Fig. 5b shows the pH measured *in vivo* (average and standard deviation), where the horizontal dashed line shows the assumed *in vivo* blood pH value of 7.45. Similar to the temperature sensors, failure at different times resulted in unequal datapoints in each group. The dashed vertical line at 3 h is the last time at which both Ti sensors functioned (one Ti sensor never recorded) and at 17 h is the last timepoint where all three Mg pH sensors recorded. For all recordings made after implantation, the average pH above the Mg plates was 7.4 ± 0.8 (n = 83), and the average pH above the Ti plates was 6.6 ± 0.4 (n = 21). It can be seen that the Mg pH is stable for the first 15 h, and then tends towards increasing values (maximum pH recorded is 9.37). Based on a two-way ANOVA, the pH depends significantly on material type ($p < 0.001$) and implantation time ($p < 0.001$), with an interaction between them.

3.7. Strain and 3D movement

Dynamic loading was analyzed for one broken and one intact magnesium plate and the contralateral titanium plates (no dynamic loading was recorded in the third animal on either plate).

Starting with the non-broken Mg plate (animal 1), the peak strains were extracted for two recording periods of Mg (6 and 10 h after activation) and Ti (6 h after activation). Fig. 6a and b shows the strains recorded 6 h after activation, with the calculated peak strains labeled (black circles), and Fig. 6c and d shows the corresponding accelerometer recordings. Fig. 6e and f shows bar plots representing the peak strains calculated for each dynamic loading period of Mg and Ti, respectively. The average peak strains across all dynamic periods are shown in Table 4.

For animal 2, the dynamic peak strains for each period are shown in Fig. 7 for Mg (a) and Ti (b); periods where no chewing was detected are left blank in the plots. The strain readings for Ti were only possible for 22 h versus 87 h for Mg. The average peak strains for the titanium plate are shown in Table 4 and are slightly smaller than those of animal 1. Around 25 h after activation, there is a large shift in the Mg dynamic peak strain towards zero. This presumably corresponds to the point of plate failure, as the plate is no longer able to fully carry the load.

Fig. 8a–d shows the plate strains for a period before failure (at 18 h) and after failure (at 40 h) of animal 2 with the corresponding accelerometer data; Fig. 8e shows the boxplot of all peak strains recorded before and after failure, with the inset depicting a microCT 3D render of the plate and sensors as scanned after explantation. There is a change in both the magnitude and direction of strain before and after failure (see

Table 3
Recording times of each sensor. Due to cable failure at various timepoints, sensors recorded for differing lengths of time. Two temperature sensors were placed at each implantation site at a refence location (ref) and close to the caudal osteotomy line (ost). Measurement points recorded before implantation are also considered in the table. * denotes recording until sacrifice.

Device	pH [hours]	Temperature (ref, ost) [hours]	Strain [hours]	Accelerometer [days]
Sheep 1, Mg	27	169, 31	10	26.3
Sheep 1, Ti	7	278, 15	7	19.8
Sheep 2, Mg	45	106, 101	87	12.7
Sheep 2, Ti	20	678*, 87	22	28.3*
Sheep 3, Mg	21	327, 80	5	21.3
Sheep 3, Ti	–	119, 119	4	18.7

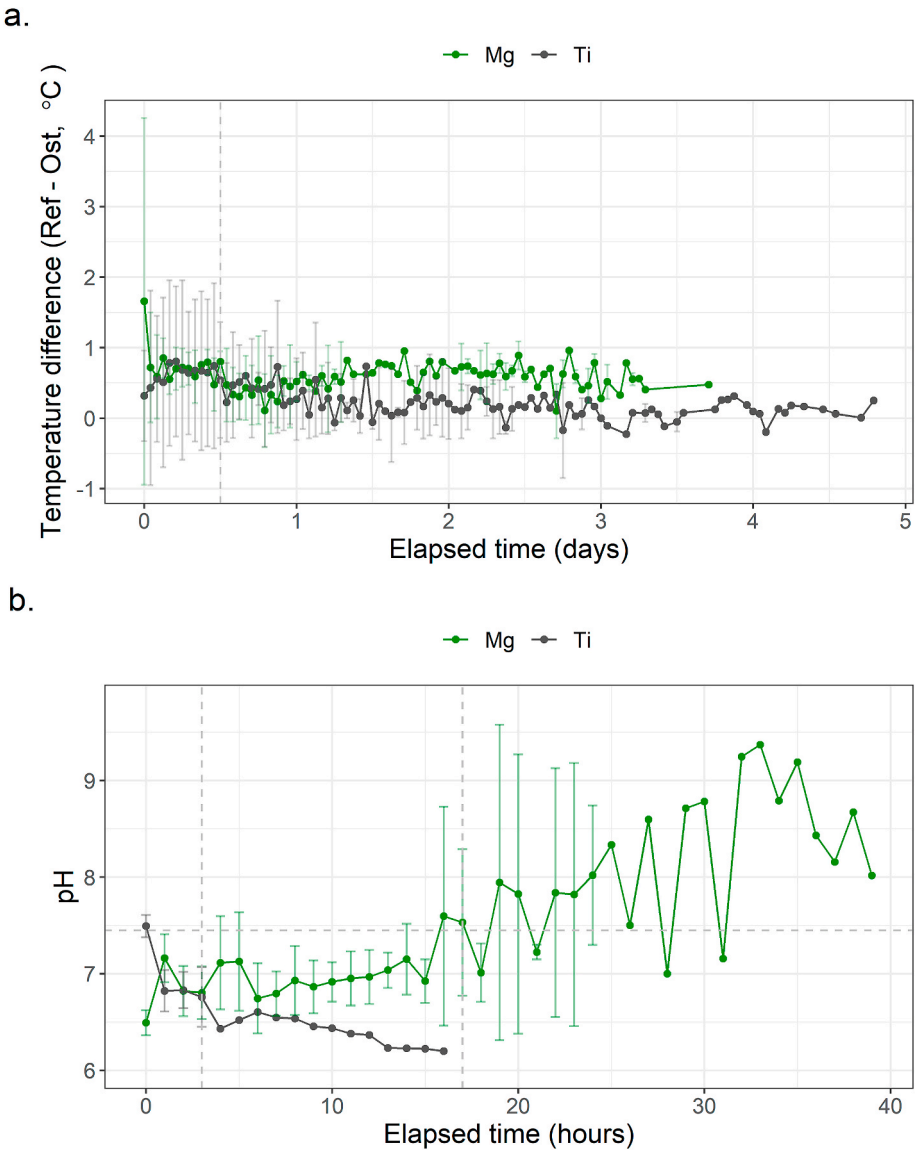

Fig. 5. ***In vivo*** **temperature and pH measurements.** a) Mean and standard deviation of the temperature difference (reference – osteotomy) for each implantation site separated by material type averaged across all three sheep. Only timepoints after implantation where both sensors (reference and osteotomy sensor) recorded data were included. The dashed vertical line at 12 h represents the last timepoint at which all temperature sensors were functioning (12 sensors total). The osteotomy sensors were above the caudal cut line and the reference sensors were placed approximately 60 mm away. In all cases, the reference temperature was higher than the osteotomy temperature on average. b) Mean and standard deviation of pH measured above Mg and Ti plates for timepoints after implantation, averaged across all sheep. The dashed horizontal line represents an assumed *in vivo* pH of 7.45. The dashed vertical line at 3 h is the last time at which both Ti sensors functioned (one Ti sensor never recorded) and at 17 h is the last timepoint where all three Mg pH sensors recorded. Datapoints without an error bar indicate that only one sensor functioned (or, in the case of temperature, one set of temperature sensors).

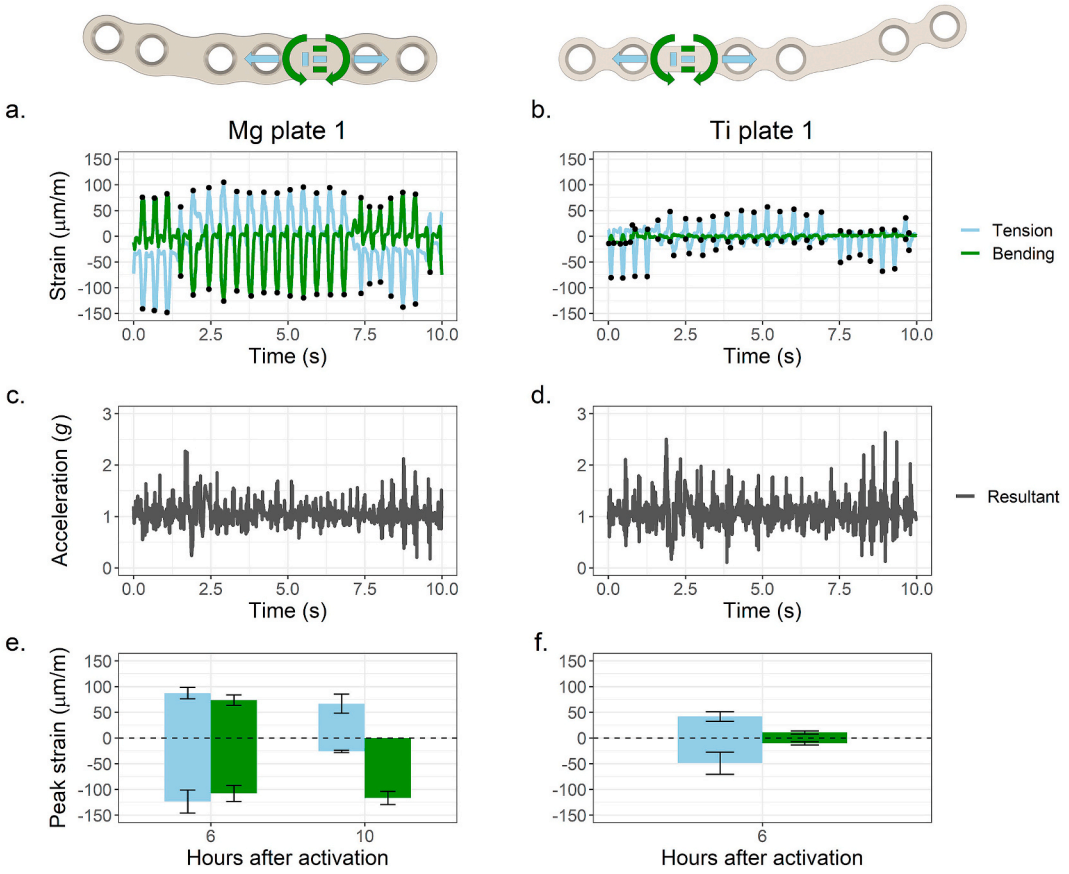

Fig. 6. Strains recorded after 6 h of activation for animal 1. 10 s of data recorded for a) Mg- and b) Ti-plates with the calculated peak strains labeled. Top: Corresponding measurement directions (arrows indicate positive direction). c, d) Accelerometer recordings made during the same measurement period. e, f) Bar plots of peak strain (mean and standard deviation) in the positive and negative directions for all identified dynamic loading periods.

Table 4
Mean ± standard deviation (*n*) of calculated peak strains (in µm/m) recorded during all dynamic loading periods for Mg and Ti plates. The results are grouped by loading direction. For Mg plate 2, the results are further separated by intact (before the plate broke) and broken plates.

	Tension-	Tension+	Bending-	Bending+
Mg 1	−72.2 ± 52.3 (19)	76.6 ± 18.4 (27)	−112.2 ± 14.6 (28)	73.6 ± 10.1 (9)
Mg 2 intact	−376.6 ± 234.3 (163)	–	−91.4 ± 31.4 (148)	7.2 ± 3.4 (30)
Mg 2 broken	−41.2 ± 21.3 (357)	52.3 ± 30.2 (427)	−11.9 ± 6.8 (218)	11.7 ± 5.3 (489)
Ti 1	−49.0 ± 21.5 (17)	41.8 ± 9.5 (15)	−10.4 ± 3.1 (19)	10.7 ± 2.8 (9)
Ti 2	−16.0 ± 9.4 (131)	29.7 ± 22.9 (220)	−7.3 ± 5.2 (130)	4.5 ± 2.6 (181)

Table 4 and Fig. 8a and b), while the accelerometer data is consistent in both cases (Fig. 8c and d). Differences in plate placement (Fig. 9) or animal behavior could have contributed to the altered loading magnitude and direction of plate 2, which presumably led to its failure.

4. Discussion

In this study, we developed and implemented a fully implantable measurement system to record temperature, pH, and strain data from Mg and Ti plates *in vivo*, using a sheep zygomatic arch defect model with the goal of quantifying the complex mechanical and environmental conditions affecting Mg degradation and fracture healing. To successfully carry out the strain measurements on a degrading surface *in vivo*, we first tested different coating options that would allow the strain gauges to remain attached to the plate while being in the body. The hybrid coating of PEO + parylene-C significantly reduced wear volume and increased the critical loads in scratch tests compared to only parylene-coated samples. Even after immersion in SBF, the wear volume did not significantly increase, indicating good protection of the PEO-coated substrate by parylene after exposure to the harsh environment that may be expected for the *in vivo* conditions. Cohesive and adhesive failure loads (L_{C1} and L_{C2}) were both increased for the hybrid samples, indicating improved adhesion of parylene to the PEO-coated substrates. This may be attributed to the rough, porous surface texture, which has been shown to greatly increase adhesion of parylene to titanium substrates [50]. Additionally, samples that were hybrid-coated with PEO + parylene-C and then immersed were fully protected from degradation (see Fig. S2, supplementary information). This is likely due to the combined effect of PEO coating decreasing reactivity of the Mg substrate, coupled with the increased adhesion of parylene on the PEO surface. Additionally, any pores or defects in the PEO coating may have been covered by the parylene, further improving corrosion resistance [35,55]. This demonstrates that Mg degradation can be reduced (and even completely prevented temporarily) with this hybrid coating, potentially allowing strain gauges to remain bonded to the surface and sufficiently protecting the sensors. The hybrid coating was considered safe for *in vivo* application based on these results.

While the combination of polyurethane and parylene-C coating could

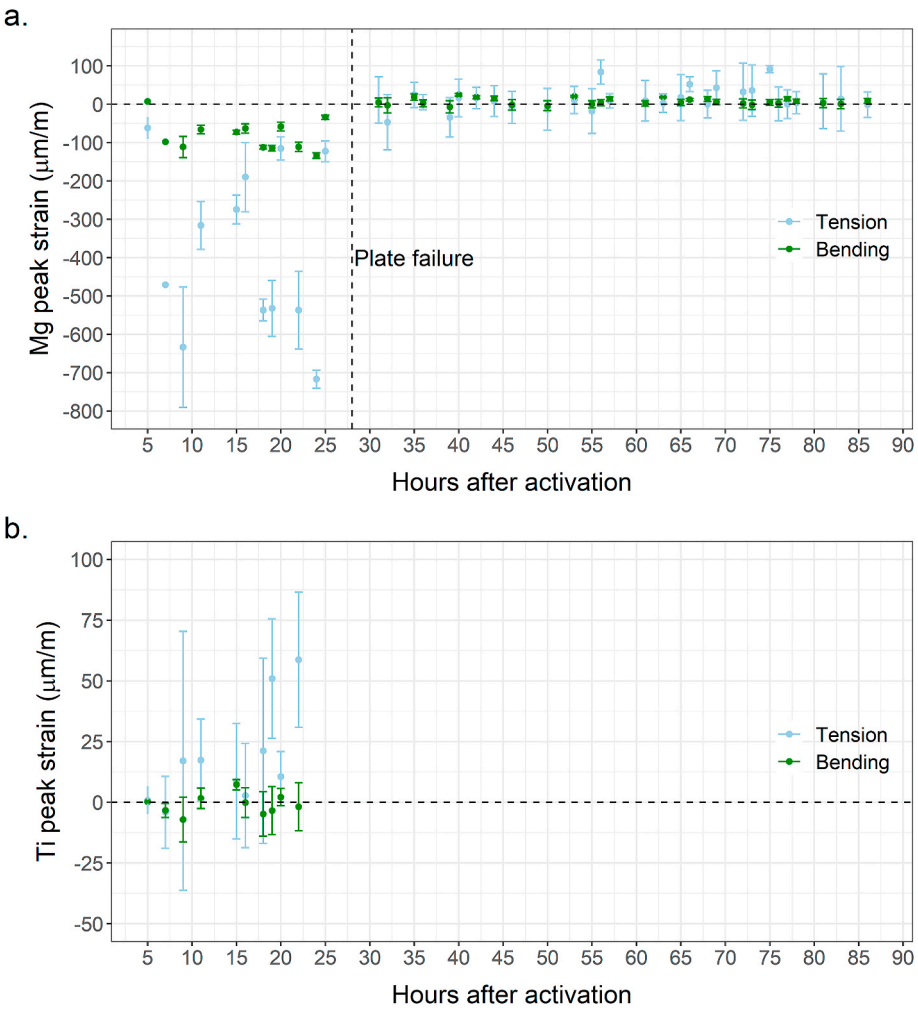

Fig. 7. Mean and standard deviation peak strains calculated during the dynamic loading periods for animal 2. a) Peak strains for Mg plate 2 recorded over 87 h. b) Peak strains for Ti plate 2 recorded for 22 h. Gaps in the data indicate periods in which no dynamic loading was detected (i.e., only static loading with no peaks). Based on the sudden change in strain magnitude and direction, plate failure is presumed to occur between 25 and 31 h (dashed vertical line = 28 h).

sufficiently protect the soldered sensors and cables *in vitro*, the constant motion from chewing *in vivo* resulted in cyclic loading on the parylene-coated cables, eventually forming cracks in the parylene and allowing water to penetrate. Since the cables are not inherently waterproof, this eventually damaged the copper traces carrying the electrical signals, presumably causing eventual sensor failure and premature battery death. This is especially apparent from the recording times of the sensors (Table 3), which shows the sensors with longest cables (pH, strain, osteotomy temperature) to record the shortest time. As they had longer cables fixed at one end, they were subjected more to loading. Additionally, the titanium case was placed subcutaneously and free to move, increasing the motion of the cables. On the other hand, the strain gauges remained glued to the plate surfaces and the solder joints, protected additionally with polyurethane, appeared undamaged, and no fluid penetrated the titanium case. In all cases, the accelerometer recorded the longest, because it was housed inside the titanium case. Based on the energy consumption and data storage capabilities, the measurement system is capable of recording at least twice as long as the planned 8-weeks lifetime while measuring once per hour, assuming no cable failure.

Immersion in SBF showed that the Ti cases remained sealed and no water penetrated the cases. The strain and temperature sensors were capable of measuring for >60 days (loaded and unloaded) in a 37 °C oven. The calibration was measured before and after with generally <1 % change in sensitivity. The resistors soldered to a stretchable cable, and covered with polyurethane plus parylene and subsequently immersed in simulated body fluid, remained stable for the entire *in vitro* test duration of 3 weeks. Based on these results, we generally deem the sensors stable enough for *in vivo* applications. Future studies utilizing these measurement techniques while preventing cable damage may provide further useful insights into the effects of bioresorbable Mg implants on fracture-fixation applications. Stability of the cables could be improved by applying the polyurethane coating along the entire length of the cable and rigidly fixating the titanium case to reduce cable motion, or investigating other cable and coating materials.

One goal of this study was to determine if there is a local temperature change at the osteotomy site. In general, the reference temperature was found to be higher than the osteotomy temperature. The reference temperature was 0.28 °C higher than the osteotomy temperature for the Ti plates ($p < 0.01$, $n = 167$) and 0.59 °C higher for the Mg plates ($p < 0.001$, $n = 148$). The results and their implications on fracture healing are limited by the short recording time and lack of osteotomy healing in the present study. Haluzan et al. reported that the peak temperature difference between reference and fracture locations should occur after three weeks [61], whereas the current osteotomy sensors could only record for five days. However, a recent study reported that bone nonunion (i.e., non-consolidated fracture) leads to initially colder temperatures and could indicate an interruption of bone healing [10]. This may be supported by our results, which showed a lower osteotomy temperature versus reference temperature and also a lack of osteotomy

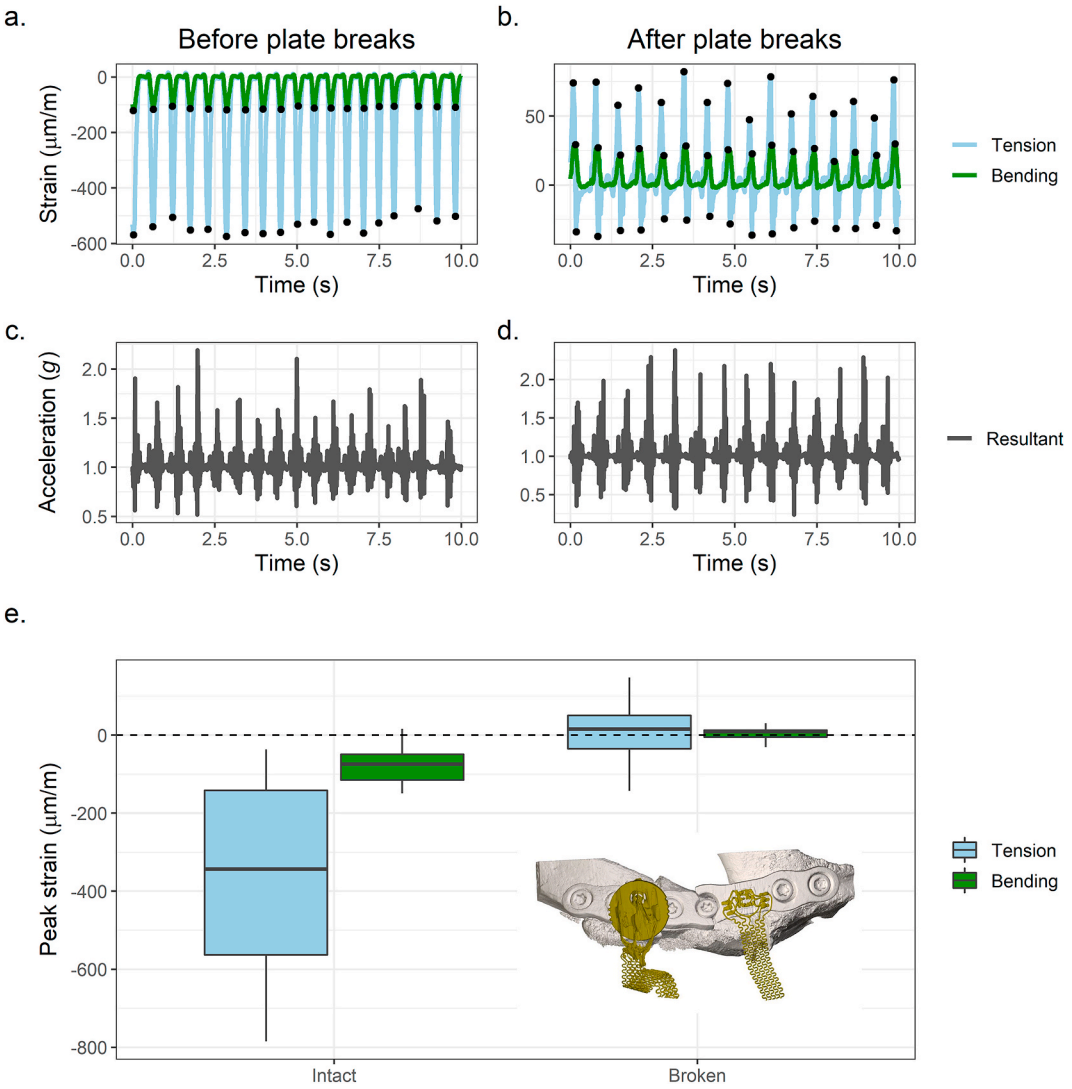

Fig. 8. Contrasting strain measurements before and after breakage of Mg plate 2. 10 s of strain data recorded a) before and b) after the Mg plate broke, with the calculated peak strains labeled. c, d) Resultant accelerometer recordings made during the corresponding periods, revealing similar data. e) Boxplots of all calculated peak strains before and after plate breaking during dynamic loading periods. Inset: MicroCT scan of plate 2 after explantation; the plate is broken at the third most ventral screw location on the mobilized bone fragment.

consolidation. Furthermore, Epari et al. reported that the temperature in a fractured sheep tibia was initially lower than the normal body temperature, possibly due to damaged blood supply, and never increased to the expected body temperature within 10 days [62]. Future studies should aim for longer recording times in the vicinity of healing bone to gather more localized data regarding the thermal changes during bone healing.

The *in vivo* pH in the vicinity of Mg and Ti plates was measured in this study, providing insight into the effects of Mg degradation and the body's response to injury. Within hours after implantation, the pH above the Ti plates stayed in the range of 6–7 and showed a decreasing trend (Fig. 5b) [7]. A previous study measuring pH changes between 4 and 48 h in a rat osteotomy hematoma found average pH values of 6.62 ± 0.33 [7], which is in good agreement with the average pH above the titanium plates found in this study (6.6 ± 0.4). Because the pH sensors were placed above the caudal osteotomy gap, it is likely that the pH decrease seen in the present study is a result of the body's healing response or damaged blood vessels, leading to hypoxic conditions and increased lactic acid production, as reported in Ref. [7]. In the present study, the Ti pH sensors failed sooner than the Mg pH sensors, with one not recording any data (Table 3). This could be because the Ti plates are dimensionally smaller than the Mg plates, making the contact area of the pH clamps smaller and potentially less stable. The reference electrodes could have been damaged if they shifted after implantation, preventing further measurements. Even though the pH above the Ti plates was only measured for 16 h, it still has interesting implications on implant development and represents the initial stage of interaction with the body.

For the Mg plates, the pH initially stayed between 6.5 and 7.5 and showed an increasing trend within the first 15 h, exceeding the pH above the Ti plates. A recent *in vitro* study found that for non-PEO coated Mg–Ca alloys immersed for 12 h with conditions mimicking the *in vivo* environment, the pH close to the surface (50 μm) stayed below 8.2 [2]. However, these tests performed on non-PEO coated plates make a direct comparison to the present results impossible, because a PEO-coated plate dissolves slower and thus a smaller pH increase is expected in the present case. Another study measured the local pH 40 μm above PEO-coated Mg for 72 h *in vitro* in minimum essential medium (MEM) and found that the pH ranged from 7.2 to 8.4 after 30 h of immersion, with signs of PEO-coating dissolution starting after 6 h [55]. This is seemingly in agreement with our *in vivo* results, which exhibited a similar pH range at timepoints after 15 h. However, one limitation of our

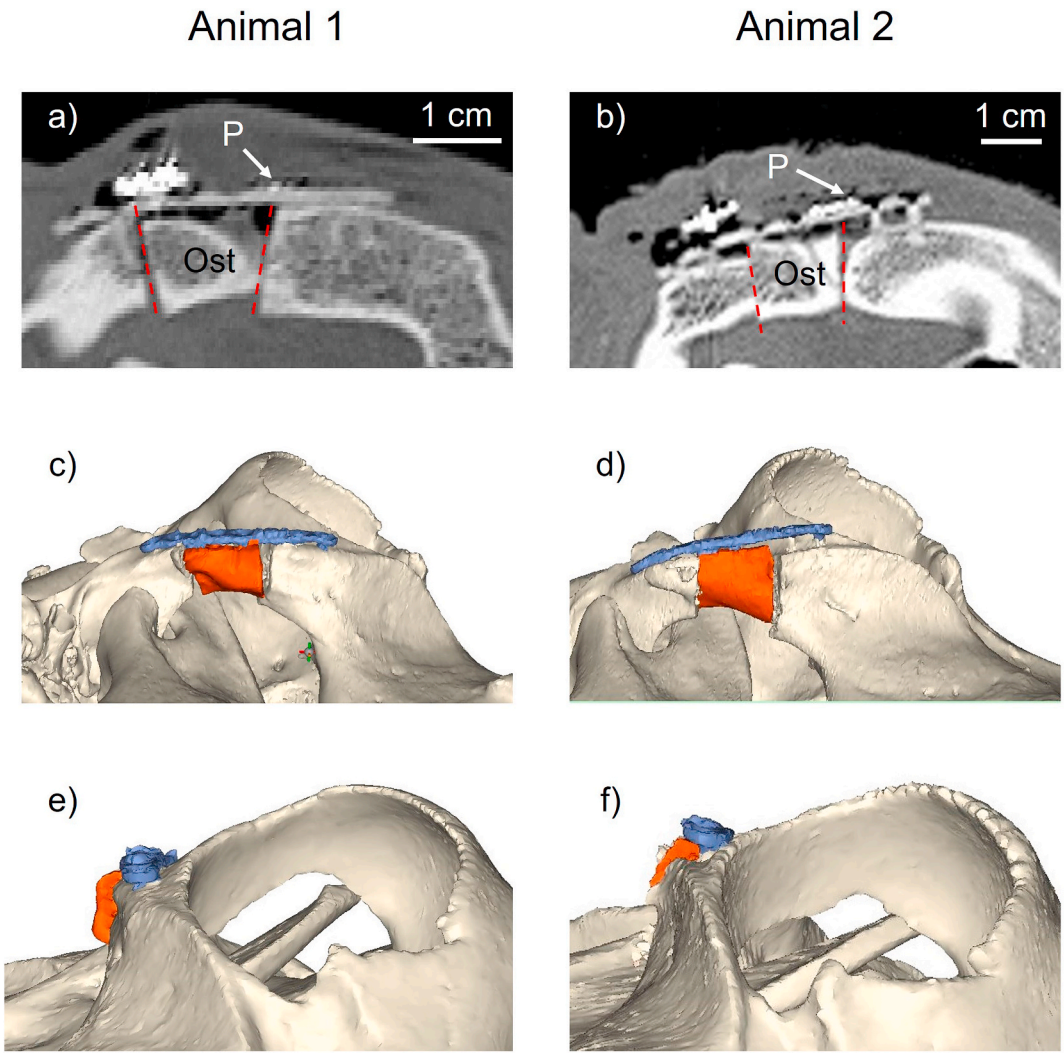

Fig. 9. Post-operative CT scans of Mg plates **from animals 1 and 2.** a, b) Ventral view of the plate (P) and osteotomy (Ost) from the post-operative CT scans of animal 1 (a) and 2 (b). c, d) 3D reconstructions, illustrating how the plates were placed in relation to the zygomatic arch bone and osteotomy; plate 2 is not fully flush with the bone on the rostral side. e, f) The rostral view shows that the top of plate 2 could have been in contact with the orbital bone; these factors may have altered the loading magnitude and direction of plate 2, contributing to plate breaking.

study is that while a clamp was used to fixate the pH sensors to the plate, it did not entirely limit motion of the sensors; this could lead to a changing distance between the sensor and the plate (with a range between 0.5 mm and 2 mm), which is known to affect pH measurements [2,4]. Fluid flow also affects the pH around the degrading plate [2], and while we do not know the exact values *in vivo*, the near-constant animal chewing and increased blood flow to bone after injury [63] indicates that there is not a static fluid environment in the vicinity of the plate. If the fluid is not circulating as freely as without the pH sensor in place, the pH increase may result from the lack of fluid exchange, preventing the delivery of new elements, such as Ca and P, that may help forming a protective corrosion product layer [2]. Nevertheless, despite these limitations, the pH values presented here appear to be in a reasonable range based on *in vitro* studies and support the notion that pH does not initially increase to highly alkaline levels *in vivo* for PEO-coated plates. Furthermore, our study shows that Mg degradation can lead to slightly increased pH *in vivo* compared to Ti implants.

After 15 h, the pH strongly increases, reaching a maximum value of 9.5 (Fig. 5b). In the previously mentioned *in vitro* study, a maximum pH of 9 was obtained approximately 50 h after immersion [55], while in the present *in vivo* study values between 9 and 9.5 were reached after 37 h. This pH increase could be due to the PEO coating dissolving over time, leading to higher Mg degradation and thus higher pH. Previous studies in our group found the degradation rate of the PEO-coated X0 plates after implantation for 8 weeks *in vivo* to be between 0.2 and 0.4 mm/year [60,64,65]. However, due to the study design, it is impossible to know how much the plates degraded within 1–2 days. Additionally, the plates in this study were bent (i.e. plastically deformed) after PEO coating at the location where the pH sensor was placed to enable better fitting to the bone. This could have damaged the coating at the measurement point, leading to faster degradation and rising pH if the Mg substrate was exposed. After 15 h, the error bars of the pH measurement also began to increase (Fig. 5b). Besides possible PEO-coating dissolution, this could be due to drift, tissue on-growth, and/or hydrogen-gas bubbles from implant degradation that potentially impact the recordings. Lab testing showed the drift to be less than 0.01 pH/day in SBF. Previous studies using ISFET sensors *in vivo* indeed reported issues with drift in the hours and days after implantation [66,67], with one device being able to record successfully for 21 h *in vivo* [68]. Upon explantation of our sensors after 8 weeks, fibrous encapsulation was found around the plates and pH sensors, which could prevent measurements of the plates' pH. Within the 39-h recording time of our study, proteins and neutrophils may have started to adsorb on the pH sensor as part of a foreign-body reaction [69,70], which could affect the

measurement. Because the reference (Ti) pH sensor did not record as long, it is difficult to conclude if this increase in Mg pH was a result of a change to the Mg plate (such as degradation of the PEO coating) or adsorption of proteins, immune response, and/or hydrogen-gas formation. It might be possible to limit this effect in the future by applying a protective but still ion-conducting polymer, such as Nafion, to protect the sensor [71].

In general, surgeries and sensor implantations were carried out successfully. In one case, the sheep had to be sacrificed prematurely after four weeks for reasons unrelated to the operation; this was coincidentally also the animal with the broken plate. Additionally, it was found that none of the osteotomies had healed after eight weeks. This was the case for both the Mg and Ti implants and is apparently not related to the material type. It could be that the loading on the bone was too high, even when fixated with a Ti plate, due to the size of the osteotomy gap and movement of the fragment, especially if chewing rotated the defect and produced shear movement or if the fixation was not rigid enough [19,21]. Recently, a study using Mg and Ti plates for fracture fixation in the mandibles of different minipig breeds showed that those with higher chewing forces led to instabilities in both types of plates, supporting the hypothesis that plate loading could have been too high to allow for bone healing in the present study [72].

The Mg plates exhibited generally higher strains than the Ti plates in both loading directions (Table 4). This may be due to different material properties, geometrical constraints, and/or the behavior of the specific sheep. Under equivalent loading, there will be less strain on the Ti plate due to its higher Young's modulus. On the other hand, the Ti plate was smaller than the Mg plate, which would cause higher strains on the Ti plate, compared to one having the same geometry as the Mg implant. Because the Mg and Ti plates were on contralateral sides, one side may have experienced higher loading due to different muscle activation during mastication. Both positive and negative strains were recorded during the chewing cycles in animal 1 (Fig. 6a), which is due to the sheep chewing not always on the same side of the mouth, causing the load to change direction when they chew on an opposite side. Additionally, these readings are only representative of the initial loading state, as they were recorded within 10 h (animal 1) to 25 h (animal 2 before plate breakage) of implantation. Nevertheless, the presented results provide *in vivo* loading data that is currently lacking in the literature. This allows for improvements in material and implant design, and may also be used to create data-driven *in vitro* tests and simulations.

The data collected also elucidates the probable cause of plate failure in animal 2. Because the Ti strains are similar in animals 1 and 2, differences in animal behavior are probably not the cause of failure. The fact that the accelerometer data are similar before and after assumed plate breaking (Fig. 8c and d) supports the hypothesis that the plate broke between periods 25 and 31, and not that the sudden change in strain was caused by e.g. changes in the chewing pattern. As listed in Table 4, the average strain before failure in animal 2 (-376.6 ± 234.3 μm/m tension-) was much higher than in animal 1 (-72.2 ± 52.3 μm/m tension-) for the Mg plate. Thus, premature plate failure has been presumably caused by higher-than-expected loading rather than via excessive corrosion or stress corrosion cracking. The directions of strain for animal 1 and 2 were also different. For animal 1, the magnitudes and directions for tension and bending are similar, while for animal 2 they both tend strongly towards the negative direction (Table 4). This could be caused by the orientation of the plate during implantation, potentially due to insufficient pre-bending or the challenging surgical placement. Fig. 9 shows clinical CT scans taken immediately after surgery. The top of plate 2 appears to be in contact with the orbital bone (Fig. 9f), rather than lying flatly on the zygomatic arch as plate 1 did (Fig. 9e). The gap, which was already visualized immediately after surgery before plate breakage, has probably prevented the screws from being fully inserted (Fig. 9d) and thus caused the plate to bend towards the medial direction when the masseter muscle acted on the zygomatic arch defect. This would produce a strong compressive (negative tension) strain on the top surface of the plate, as indicated by the data in Table 4 and Fig. 8e, and alter the loading magnitude and direction of plate 2, eventually causing plate breakage.

One limitation of using strain gauges to characterize the magnesium plates is that the gauged area is covered with polyurethane and parylene coatings, preventing the magnesium from degrading. This could lead to inaccurate measurements if there are large geometrical changes outside of the coated area, with the plate not being measured in the degraded state. Based on the microCT data, no geometrical changes outside the coated area were visible, likely because the degradation rate is slow, with the implant surface not changing significantly within 24 weeks of implantation [73]. As the longest strain recording was only 87 h, the effects of degradation are negligible. Nevertheless, we were still able to measure interesting differences based on the material (Mg vs Ti) and how it was implanted (see previous discussion). Preventing Mg degradation could also provide an interesting opportunity for future research by allowing the mechanical and biological effects of Mg to be decoupled; for example, the effect of Mg's lower Young's modulus on stress shielding could be directly measured. Gathering data on the initial, uncorroded loading state of Mg plates could also provide useful information for implant design, for example as input data to FE models for the adjustment of design parameters. In the future, additional *in vivo* tests with sufficient sample size should be performed with the sensors presented in this work, to allow for further quantification of strain, pH and temperature, and improved verification of the results.

5. Conclusions

In this study, we developed and implemented a custom-designed, fully-implantable measurement system to record *in vivo* data from Mg and Ti plates used for fracture fixation for the first time. These new sensors seamlessly integrated into a low-power sensor node, providing unparalleled accuracy during long-term evaluations. The data accumulated provides detailed information regarding the mechanical loading of plate implants *in vivo* and quantifies the degradation environment that strongly affects biodegradable implants. Using these results, the design and characterization of Mg implants can be improved, thus increasing their potential for use in clinical practice.

The pH above titanium plates was slightly lower than the assumed *in vivo* pH of 7.4, likely due to the effects of the osteotomy. This insight may have important implications on currently used *in vitro* test conditions for Mg alloys designed for fracture-fixation applications, as the *in vivo* pH may be lower than anticipated due to the osteotomy. The pH 1–2 mm above magnesium plates was slightly elevated in comparison, but stayed generally under 7.4 for the first 15 h. The results indicate that Mg degrading *in vivo* does not produce strong alkalization, especially when the Mg implant is PEO coated. These results further highlight the need for laboratory testing to closely mimic the *in vivo* conditions to get the most reliable results.

The PEO + parylene hybrid coating improved tribological properties of the Mg alloy and allowed for strain gauges to adhere to the degrading Mg surface *in vivo*. Improvements to the cable- and material coating should be made for long-term recordings in the future. Strain readings allowed for the determination of dynamic loading that the plates experienced during chewing. The strains in the Mg plates were higher than in the Ti implants, but no effects on bone healing could be determined. Premature plate failure of one Mg plate could be attributed to the high strains measured in this implant and ascribed to an implant misfit upon surgery.

In conclusion, our results reveal that it is possible to record in detail the environmental and mechanical parameters that affect biodegradable implants *in vivo*. This enhances our understanding of these resorbable materials and enables their improvements for clinical applications.

Ethics approval and consent to participate

Experiments were performed in accordance with Swiss laws of animal protection and welfare and were approved by the Cantonal Veterinary Office of Zurich (license number ZH 121/20).

CRediT authorship contribution statement

A.M. Rich: Writing – review & editing, Writing – original draft, Visualization, Software, Methodology, Investigation, Formal analysis, Conceptualization. **W. Rubin:** Writing – review & editing, Investigation, Formal analysis. **S. Rickli:** Writing – review & editing, Software, Methodology, Investigation, Formal analysis. **T. Akhmetshina:** Writing – review & editing, Investigation. **J. Cossu:** Writing – review & editing, Visualization, Investigation, Formal analysis. **L. Berger:** Writing – review & editing, Validation, Supervision, Project administration, Conceptualization. **M. Magno:** Writing – review & editing, Methodology. **K.M. Nuss:** Writing – review & editing, Validation, Project administration, Methodology. **B. Schaller:** Writing – review & editing, Project administration, Methodology, Conceptualization. **J.F. Löffler:** Writing – review & editing, Validation, Supervision, Project administration, Methodology, Funding acquisition, Conceptualization.

Declaration of competing interest

None.

Acknowledgements

The authors would like to thank Dr. Philipp Mayer of ETH Zurich for providing valuable feedback on PCB design, Dr. Giuseppe Tussiwand of HAPTICA SRL for the guidance on using semiconductor strain gauges, Sebastian Reitz of ETH Zurich for producing intricate sensor components, and Dr. Thomas Imwinkelried from RMS Foundation for assisting with the PEO coating. This work was supported by the Swiss National Science Foundation via an SNF Sinergia Grant (grant number CRSII5-180367).

Appendix A. Supplementary data

Supplementary data to this article can be found online at https://doi.org/10.1016/j.bioactmat.2024.09.015.

References

[1] J. Gonzalez, R.Q. Hou, E.P.S. Nidadavolu, R. Willumeit-Römer, F. Feyerabend, Magnesium degradation under physiological conditions – best practice, Bioact. Mater. 3 (2) (2018) 174–185, https://doi.org/10.1016/j.bioactmat.2018.01.003.
[2] C. Wang, et al., Low interfacial pH discloses the favorable biodegradability of several Mg alloys, Corrosion Sci. 197 (December 2021) (2022) 110059, https://doi.org/10.1016/j.corsci.2021.110059.
[3] J. Gonzalez, et al., Mg biodegradation mechanism deduced from the local surface environment under simulated physiological conditions, Adv. Healthcare Mater. 10 (13) (2021), https://doi.org/10.1002/adhm.202100053.
[4] S.V. Lamaka, J. Gonzalez, D. Mei, F. Feyerabend, R. Willumeit-Römer, M. L. Zheludkevich, Local pH and its evolution near Mg alloy surfaces exposed to simulated body fluids, Adv. Mater. Interfac. 5 (18) (2018) 1–6, https://doi.org/10.1002/admi.201800169.
[5] J. Greenbaum, M. Nirmalan, Acid-base balance: the traditional approach, Curr. Anaesth. Crit. Care 16 (3) (2005) 137–142, https://doi.org/10.1016/j.cacc.2005.03.009.
[6] S.L. Percival, S. McCarty, J.A. Hunt, E.J. Woods, The effects of pH on wound healing, biofilms, and antimicrobial efficacy, Wound Repair Regen. 22 (2) (2014) 174–186, https://doi.org/10.1111/wrr.12125.
[7] J.C. Berkmann, et al., Early pH changes in musculoskeletal tissues upon injury—aerobic catabolic pathway activity linked to inter-individual differences in local pH, Int. J. Mol. Sci. 21 (7) (2020), https://doi.org/10.3390/ijms21072513.
[8] I. Bartsch, E. Willbold, B. Rosenhahn, F. Witte, Non-invasive pH determination adjacent to degradable biomaterials in vivo, Acta Biomater. 10 (1) (2014) 34–39, https://doi.org/10.1016/j.actbio.2013.08.047.
[9] N.T. Kirkland, J. Lespagnol, N. Birbilis, M.P. Staiger, A survey of bio-corrosion rates of magnesium alloys, Corrosion Sci. 52 (2) (2010) 287–291, https://doi.org/10.1016/j.corsci.2009.09.033.
[10] W. auf der Strasse, D.P. Campos, C.J.A. Mendonça, J.F. Soni, J. Mendes, P. Nohama, Evaluation of tibia bone healing by infrared thermography: a case study, J. Multidiscip. Healthc. 14 (2021) 3161–3175, https://doi.org/10.2147/JMDH.S330094.
[11] E.F. Morgan, G.U. Unnikrisnan, A.I. Hussein, Bone mechanical properties in healthy and diseased states, Annu. Rev. Biomed. Eng. 20 (2018) 119–143, https://doi.org/10.1146/annurev-bioeng-062117-121139.
[12] Titanium Alloy Ti 6Al-4V." Accessed: November. 16, 2020. [Online]. Available: https://cartech.ides.com/datasheet.aspx?i=101&E=269.
[13] R. Karunakaran, S. Ortgies, A. Tamayol, F. Bobaru, M.P. Sealy, Additive manufacturing of magnesium alloys, Bioact. Mater. 5 (1) (2020) 44–54, https://doi.org/10.1016/j.bioactmat.2019.12.004.
[14] B.S. Klosterhoff, et al., Wireless sensor enables longitudinal monitoring of regenerative niche mechanics during rehabilitation that enhance bone repair, Bone 135 (December 2019) (2020) 115311, https://doi.org/10.1016/j.bone.2020.115311.
[15] M. Windolf, et al., Continuous implant load monitoring to assess bone healing status—evidence from animal testing, Medicina 58 (7) (2022), https://doi.org/10.3390/medicina58070858.
[16] J.G. Wolynski, et al., Utilizing multiple BioMEMS sensors to monitor orthopaedic strain and predict bone fracture healing, J. Orthop. Res. 37 (9) (2019) 1873–1880, https://doi.org/10.1002/jor.24325.
[17] M. Ernst, H. Baumgartner, S. Döbele, D. Höntzsch, T. Pohlemann, M. Windolf, Clinical feasibility of fracture healing assessment through continuous monitoring of implant load, J. Biomech. 116 (2021) 110188, https://doi.org/10.1016/j.jbiomech.2020.110188.
[18] C. Conceição, A. Completo, M.P. Soares dos Santos, Altering the course of fracture healing monitoring, Biomed. Eng.Adv. 5 (2023) 100068, https://doi.org/10.1016/j.bea.2022.100068. November 2022.
[19] B. Wildemann, et al., Non-union bone fractures, Nat. Rev. Dis. Prim. 7 (1) (2021), https://doi.org/10.1038/s41572-021-00289-8.
[20] B. Ganse, et al., Concepts and clinical aspects of active implants for the treatment of bone fractures, Acta Biomater. 146 (2022) 1–9, https://doi.org/10.1016/j.actbio.2022.05.001.
[21] L. Claes, Improvement of clinical fracture healing – what can be learned from mechano-biological research? J. Biomech. 115 (2021) 110148 https://doi.org/10.1016/j.jbiomech.2020.110148.
[22] G. Merle, T. Miclau, A. Parent-Harvey, E.J. Harvey, Sensor technology usage in orthopedic trauma, Injury 53 (2022) S59–S63, https://doi.org/10.1016/j.injury.2022.09.036.
[23] A.P. Baumann, et al., FDA public workshop: orthopaedic sensing, measuring, and advanced reporting technology (SMART) devices, J. Orthop. Res. 39 (1) (2021) 22–29, https://doi.org/10.1002/jor.24833.
[24] M. Ernst, R.G. Richards, M. Windolf, Smart implants in fracture care – only buzzword or real opportunity? Injury 52 (2021) S101–S105, https://doi.org/10.1016/j.injury.2020.09.026.
[25] J.A. Szivek, E.M. Johnson, F.P. Magee, In vivo strain analysis of the greyhound femoral diaphysis, J. Invest. Surg. 5 (2) (1992) 91–108, https://doi.org/10.3109/08941939209012426.
[26] W.C. de Jong, J.H. Koolstra, L.J. van Ruijven, J.A.M. Korfage, G.E.J. Langenbach, A fully implantable telemetry system for the long-term measurement of habitual bone strain, J. Biomech. 43 (3) (2010) 587–591, https://doi.org/10.1016/j.jbiomech.2009.09.036.
[27] L. Cai, et al., Osseosurface electronics—thin, wireless, battery-free and multimodal musculoskeletal biointerfaces, Nat. Commun. 12 (1) (2021) 1–12, https://doi.org/10.1038/s41467-021-27003-2.
[28] M.P. Soares dos Santos, et al., Towards an effective sensing technology to monitor micro-scale interface loosening of bioelectronic implants, Sci. Rep. 11 (1) (2021) 1–17, https://doi.org/10.1038/s41598-021-82589-3.
[29] C. Adam, T. Barth, M. Munch, K. Seide, W.H. Krautschncider, An electronic osteosynthesis implant for continuous load monitoring using a strain gauge, in: BioCAS 2021 - IEEE Biomedical Circuits and Systems Conference, Proceedings, 2021, pp. 1–6, https://doi.org/10.1109/BioCAS49922.2021.9644959.
[30] P. Blázquez-Carmona, M. Sanchez-Raya, J. Mora-Macías, J.A. Gómez-Galán, J. Domínguez, E. Reina-Romo, Real-time wireless platform for in vivo monitoring of bone regeneration, Sensors 20 (16) (2020) 1–23, https://doi.org/10.3390/s20164591.
[31] A.R. Burton, P. Sun, J.P. Lynch, Bio-compatible wireless inductive thin-film strain sensor for monitoring the growth and strain response of bone in osseointegrated prostheses, Struct. Health Monit. 20 (3) (2021) 749–767, https://doi.org/10.1177/1475921719831452.
[32] K.P. Iyengar, B.T.V. Gowers, V.K. Jain, R.S. Ahluwalia, R. Botchu, R. Vaishya, Smart sensor implant technology in total knee arthroplasty, J Clin Orthop Trauma 22 (2021) 101605, https://doi.org/10.1016/j.jcot.2021.101605.
[33] O.G. Vickers, et al., Is in vivo sensing in a total hip replacement a possibility? A review on past systems and future challenges, Prog. Biomed. Eng. 3 (4) (2021), https://doi.org/10.1088/2516-1091/ac1b7f.

[34] M.P. Soares dos Santos, R.M.C. Bernardo, Bioelectronic multifunctional bone implants: recent trends, Bioelectron Med 8 (1) (2022), https://doi.org/10.1186/s42234-022-00097-9.

[35] M. Kaseem, S. Fatimah, N. Nashrah, Y.G. Ko, Recent progress in surface modification of metals coated by plasma electrolytic oxidation: principle, structure, and performance, Prog. Mater. Sci. 117 (June 2020) (2021) 100735, https://doi.org/10.1016/j.pmatsci.2020.100735.

[36] N. Singh, U. Batra, K. Kumar, N. Ahuja, A. Mahapatro, Progress in bioactive surface coatings on biodegradable Mg alloys: a critical review towards clinical translation, Bioact. Mater. 19 (2023) 717–757, https://doi.org/10.1016/j.bioactmat.2022.05.009. March 2022.

[37] A. Kopp, et al., Long-term in vivo observations show biocompatibility and performance of ZX00 magnesium screws surface-modified by plasma-electrolytic oxidation in Göttingen miniature pigs, Acta Biomater. 157 (2023) 720–733, https://doi.org/10.1016/j.actbio.2022.11.052.

[38] C. Rendenbach, et al., Improved in vivo osseointegration and degradation behavior of PEO surface-modified WE43 magnesium plates and screws after 6 and 12 months, Mater. Sci. Eng. C 129 (May) (2021), https://doi.org/10.1016/j.msec.2021.112380.

[39] T. Imwinkelried, S. Beck, T. Iizuka, B. Schaller, Effect of a plasmaelectrolytic coating on the strength retention of in vivo and in vitro degraded magnesium implants, Acta Biomater. 9 (10) (2013) 8643–8649, https://doi.org/10.1016/j.actbio.2012.08.047.

[40] B. Schaller, et al., In vivo degradation of magnesium plate/screw osteosynthesis implant systems: soft and hard tissue response in a calvarial model in miniature pigs, J. Cranio-Maxillofacial Surg. 44 (3) (2016) 309–317, https://doi.org/10.1016/j.jcms.2015.12.009.

[41] B. Schaller, et al., Osteosynthesis of partial rib osteotomy in a miniature pig model using human standard-sized magnesium plate/screw systems: effect of cyclic deformation on implant integrity and bone healing, J. Cranio-Maxillofacial Surg. 45 (6) (2017) 862–871, https://doi.org/10.1016/j.jcms.2017.03.018.

[42] M. Golda-Cepa, K. Engvall, M. Hakkarainen, A. Kotarba, Recent progress on parylene C polymer for biomedical applications: a review, Prog. Org. Coating 140 (December 2019) (2020) 105493, https://doi.org/10.1016/j.porgcoat.2019.105493.

[43] C. Hassler, R.P. Von Metzen, P. Ruther, T. Stieglitz, Characterization of parylene C as an encapsulation material for implanted neural prostheses, J. Biomed. Mater. Res. B Appl. Biomater. 93 (1) (2010) 266–274, https://doi.org/10.1002/jbm.b.31584.

[44] J.P. Seymour, Y.M. Elkasabi, H.Y. Chen, J. Lahann, D.R. Kipke, The insulation performance of reactive parylene films in implantable electronic devices, Biomaterials 30 (31) (2009) 6158–6167, https://doi.org/10.1016/j.biomaterials.2009.07.061.

[45] W. Li, D.C. Rodger, E. Meng, J.D. Weiland, M.S. Humayun, Y.C. Tai, Wafer-level parylene packaging with integrated rf electronics for wireless retinal prostheses, J. Microelectromech. Syst. 19 (4) (2010) 735–742, https://doi.org/10.1109/JMEMS.2010.2049985.

[46] J. Ortigoza-diaz, et al., Techniques and considerations in the microfabrication of parylene C microelectromechanical systems, Micromachines 9 (2018) 422, https://doi.org/10.3390/mi9090422.

[47] V. Iacovacci, I. Naselli, A.R. Salgarella, F. Clemente, L. Ricotti, C. Cipriani, Stability and in vivo safety of gold, titanium nitride and parylene C coatings on NdFeB magnets implanted in muscles towards a new generation of myokinetic prosthetic limbs, RSC Adv. 11 (12) (2021) 6766–6775, https://doi.org/10.1039/d0ra07989h.

[48] H. Park, W. Choi, S. Oh, Y.J. Kim, S. Seok, J. Kim, A study on biocompatible polymer-based packaging of neural interface for chronic implantation, Micromachines 13 (4) (2022), https://doi.org/10.3390/mi13040516.

[49] S. Buchwalder, et al., An evaluation of parylene thin films to prevent encrustation for a urinary bladder pressure MEMS sensor system, Polymers 15 (17) (2023) 1–13, https://doi.org/10.3390/polym15173559.

[50] S. Staufert, P. Gutzwiller, F. Mushtaq, C. Hierold, Surface nanostructuring of Ti6Al4 v surfaces for parylene-C coatings with ultradurable adhesion, ACS Appl. Nano Mater. 1 (4) (2018) 1586–1594, https://doi.org/10.1021/acsanm.8b00081.

[51] M. Cieślik, et al., Engineering of bone fixation metal implants biointerface - application of parylene C as versatile protective coating, Mater. Sci. Eng. C 32 (8) (2012) 2431–2435, https://doi.org/10.1016/j.msec.2012.07.018.

[52] W.C. Kuo, T.C. Wu, C.F. Wu, W.C. Wang, Bioperformance analysis of parylene C coating for implanted nickel titanium alloy, Mater. Today Commun. 27 (2021) 102306, https://doi.org/10.1016/j.mtcomm.2021.102306.

[53] M.A. Surmeneva, et al., Effect of parylene C coating on the antibiocorrosive and mechanical properties of different magnesium alloys, Appl. Surf. Sci. 427 (2018) 617–627, https://doi.org/10.1016/j.apsusc.2017.08.066.

[54] M. Sasaki, et al., Effect of parylene C on the corrosion resistance of bioresorbable cardiovascular stents made of magnesium alloy 'original ZM10, Materials 15 (9) (2022), https://doi.org/10.3390/ma15093132.

[55] A.S. Gnedenkov, et al., Control of the Mg alloy biodegradation via PEO and polymer-containing coatings, Corrosion Sci. 182 (2021) 109254, https://doi.org/10.1016/j.corsci.2021.109254.

[56] J. Hofstetter, et al., Assessing the degradation performance of ultrahigh-purity magnesium in vitro and in vivo, Corrosion Sci. 91 (Feb. 2015) 29–36, https://doi.org/10.1016/j.corsci.2014.09.008.

[57] T. Imwinkelried, P. Kurze, S. Beck, D. Banerjee, T. Schwarz, Lean electrolyte for biocompatible plasmaelectrolytic coatings on magnesium implant material, Int.pat. (May 2013) WO2013070669.

[58] W.Y. Chung, et al., New ISFET interface circuit design with temperature compensation, Microelectron. J. 37 (10) (2006) 1105–1114, https://doi.org/10.1016/j.mejo.2006.05.001.

[59] M. Schinhammer, J. Hofstetter, C. Wegmann, F. Moszner, J.F. Löffler, P. J. Uggowitzer, On the immersion testing of degradable implant materials in simulated body fluid: active pH regulation using CO_2, Adv. Eng. Mater. 15 (6) (Jun. 2013) 434–441, https://doi.org/10.1002/adem.201200218.

[60] L. Berger, et al., In vivo performance of lean bioabsorbable Mg–Ca alloy X0 and comparison to WE43: influence of surface modification and alloying content, in: *Bioact Mater*, Same Volume and Issue, 2024 in press.

[61] D. Haluzan, et al., Thermal changes during healing of distal radius fractures—preliminary findings, Injury 46 (2015) S103–S106, https://doi.org/10.1016/j.injury.2015.10.046.

[62] D.R. Epari, J. Lienau, H. Schell, F. Witt, G.N. Duda, Pressure, oxygen tension and temperature in the periosteal callus during bone healing-An in vivo study in sheep, Bone 43 (4) (2008) 734–739, https://doi.org/10.1016/j.bone.2008.06.007.

[63] G.P. Ashcroft, et al., Measurement of blood flow in tibial fracture patients using positron emission tomography, J. Bone Joint Surg. 74 (5) (1992) 673–677.

[64] L. Berger, et al., In vivo comparison of ultrahigh-purified lean Mg alloys and rare-earth-containing WE43, in: 14th Biometals, Aug. 2022. Alicante, Spain.

[65] W. Rubin, et al., In vivo assessment of magnesium-based biodegradable screw-plate implants in a large-animal cranio-maxillofacial defect model, in: *15th Biometal*, Cetraro, Italy, Aug. 2023.

[66] M. Thompson, E.T. Vandenberg, In vivo probes: problems and perspectives, in: Laboratory Medicine for the Next Decade, ON, Hamilton, Oct. 1985, pp. 255–261.

[67] S.J. Schepel, N.F. de Rooij, G. Koning, B. Oeseburg, W.G. Zijlstra, In vivo experiments with a pH-ISFET electrode, Med. Biol. Eng. Comput. 22 (June) (1984) 6–11.

[68] P. Duroux, et al., The ion sensitive field effect transistor (ISFET) pH electrode: a new sensor for long term ambulatory pH monitoring, Gut 32 (1991) 240–245.

[69] L. Kämmerling, et al., Mitigating the foreign body response through 'immune-instructive' biomaterials, J Immunol Regen Med 12 (March) (2021) 100040, https://doi.org/10.1016/j.regen.2021.100040.

[70] O. Veiseh, A.J. Vegas, Domesticating the foreign body response: recent advances and applications, Adv. Drug Deliv. Rev. 144 (2019) 148–161, https://doi.org/10.1016/j.addr.2019.08.010.

[71] P. Hashemi, et al., Chronically implanted, nafion-coated Ag/AgCl reference electrodes for neurochemical applications, ACS Chem. Neurosci. 2 (11) (2011) 658–666, https://doi.org/10.1021/cn2000684.

[72] T. Imwinkelried, S. Beck, B. Schaller, Pre-clinical testing of human size magnesium implants in miniature pigs: implant degradation and bone fracture healing at multiple implantation sites, Mater. Sci. Eng. C 108 (October 2019) (2019) 110389, https://doi.org/10.1016/j.msec.2019.110389.

[73] N.G. Grün, et al., Comparison of a resorbable magnesium implant in small and large growing-animal models, Acta Biomater. 78 (2018) 378–386, https://doi.org/10.1016/j.actbio.2018.07.044.